Quarterly Report for

July - September 2001

Stanford Geothermal Program

DE-FG07-99ID13763

Table of Contents

1. RELATIVE PERMEABILITY OF FRACTURES

This research project is being conducted by Research Assistant Gracel Diomampo, Research Associate Kewen Li and Professor Roland Horne. The project reached a milestone point at the end of the quarter, and a technical report of the results has been completed.

1.1 INTRODUCTION

The mechanism of two-phase flow through fractures exerts an important influence on the behavior of geothermal reservoirs. Currently, two-phase flow through fractures is still poorly understood. In this study, nitrogen-water and steam-water experiments were done on both smooth and rough parallel plates to determine the governing flow mechanisms. The experiments were done using a glass plate to allow visualization of flow. Digital video recording allowed instantaneous measurement of pressure, flow rate and saturation. Saturation was computed using image analysis techniques.

The experiments showed that gas and liquid phases flow through fractures in nonuniform separate channels. The localized channels change with time as each phase path undergoes continues breaking and reforming due to invasion of the other phase. The stability of the phase paths is dependent on liquid and gas flow rate ratio. This mechanism holds true for over a range of saturation for both smooth and rough fractures.

The data from the experiments were analyzed using Darcy's law and using the concept of friction factor and equivalent Reynold's number for two-phase flow. For both smooth- and rough-walled fractures a clear relationship between relative permeability and saturation was seen. The calculated relative permeability curves follow Corey-type behavior and can be modeled using Honarpour expressions. The sum of the relative permeabilities does not equal one, indicating phase interference. The equivalent homogenous single-phase approach did not give satisfactory representation of flow through fractures. The graphs of experimentally derived friction factor with the modified Reynold's number do not reveal a distinctive linear relationship.

Theoretical Background

Multiphase flow in fractures is an important field of study for areas such as geothermal industry, oil recovery, isolation of nuclear and toxic waste in geological formations. At present, the governing flow mechanism for multiphase flow in fracture is still undetermined. There are two approaches commonly used in modeling multiphase flow in fractures, the porous medium approach and the equivalent homogeneous single-phase approach.

The porous medium approach treats fractures as connected two-dimensional porous media. In this model, a pore space occupied by one phase is not available for flow for the other phase. A phase can move from one position to another only upon establishing a continuous flow path for itself. As in porous media, the competition for pore occupancy

is described by relative permeability and governed by Darcy's law. Darcy's law for single-phase liquid flow is:

$$q_l = \frac{k_{abs}(p_i - p_o)}{\mu_l L} \tag{1.1}$$

where subscript *l* stands for the liquid phase, *i* for inlet and *o* for outlet; μ, *p*, *L*, *q*, k_{abs} are the viscosity, pressure, fracture length, Darcy flow velocity and absolute permeability respectively. The Darcy flow velocity is equal to

$$q = \frac{Q}{bw} \tag{1.2}$$

with *Q* as the volumetric flow rate, *b* the fracture aperture and *w* as the fracture width. Absolute permeability of the fracture is a function only of the fracture aperture (Witherspoon et al., 1980) as described in the cubic law

$$k_{abs} = \frac{b^2}{12} \tag{1.3}$$

For liquid phase in two-phase flow, Eqn. (1.1) becomes

$$q_l = \frac{k_{abs}k_{rl}(p_i - p_o)}{\mu_l L} \tag{1.4}$$

where k_{rl} is the relative permeability of the liquid phase.

Similarly, Darcy's law derived for single-phase isothermal gas flow in porous media (Scheidegger, 1974) is

$$q_g = \frac{k_{abs}(p_i^2 - p_o^2)}{2\mu_g L p_o} \tag{1.5}$$

with the subscript *g* pertaining to the gas phase.

In two-phase flow, Eqn. (1.5) becomes

$$q_g = \frac{k_{abs}k_{rg}(p_i^2 - p_o^2)}{2\mu_g L p_o} \tag{1.6}$$

with k_{rg} as the gas relative permeability. The sum of the k_{rl} and k_{rg} indicates the extent of phase interference. A sum of relative permeabilities equal to one means the absence of phase interference. Physically this implies each phase flows in its own path without impeding the flow of the other. The lower is the sum of the relative permeabilities from unity the greater is the phase interference.

Relative permeability functions are usually taken to be dependent on phase saturation. The two most commonly used expressions for relative permeability for homogeneous porous media are the X-curve and Corey curve (Corey, 1954). The X-curve describes relative permeability as a linear function of saturation

$$k_{rl} = S_l \tag{1.7}$$

$$k_{rg} = S_g \tag{1.8}$$

where S_l and S_g are the liquid and gas saturation respectively. The Corey curve relates relative permeability to the irreducible or residual liquid and gas saturation, S_{rl} and S_{rg}

$$k_{rl} = S^{*4} \tag{1.9}$$

$$k_{rg} = (1 - S^*)^2 (1 - S^{*2}) \tag{1.10}$$

$$S^* = (S_l - S_{rl}) / (1 - S_{rl} - S_{rg}) \tag{1.11}$$

The equivalent homogeneous single-phase approach treats flow through fracture as a limiting case of flow through pipes. In this model, phase velocities in a fracture are equal and capillary forces are negligible. A continuous flow path is not required for movement of each phase. A phase can be carried along by one phase as bubbles, slug or other complex structures. As in pipes, flow can be described by the concept of friction factors and using averaged properties (Fourar et al., 1993)

$$(p_i - p_o) = \frac{\Pi f \rho_m V_m^2}{2A} \tag{1.12}$$

where Π is the fracture perimeter, A is the cross sectional area to flow, ρ_m average density and V_m as average flow velocity. The average density is described by

$$\rho_m = \frac{\rho_g Q_g + \rho_l Q_l}{Q_g + Q_l} \tag{1.13}$$

The average flow velocity is equal to

$$V_m = \frac{Q_g + Q_l}{A} \tag{1.14}$$

The friction factor, f, is derived empirically as a function of the averaged Reynolds number calculated by

$$N_{\mathrm{Re}} = \frac{2bV_m \rho_m}{\mu_m} \tag{1.15}$$

with μ_m as average viscosity

$$\mu_m = \frac{\mu_g Q_g + \mu_l Q_l}{Q_g + Q_l} \tag{1.16}$$

There are several expressions used to relate friction factor and Reynolds number. The commonly used one for flow through fracture is the generalized Blasium form (Lockhart and Martinelli, 1949):

$$f = \frac{C}{N_{\mathrm{Re}}^n} \tag{1.17}$$

with C and n as constants derived from experimental data.

The validity of the two models for multiphase flow through fractures is still uncertain.

Literature Review

Only a few published data are available for two-phase flow in fractures. Most of the studies have been done for air-water or for water-oil systems. Earliest is Romm's (1966) experiment with kerosene and water through an artificial parallel-plate fracture lined with strips of polyethylene or waxed paper. Romm found a linear relationship between permeability and saturation, $S_w = k_{rw}$, $S_{nw} = k_{rnw}$ such that $k_{rw} + k_{rnw} = 1$. Fourar et al. (1993) artificially roughened glass plates with beads and flowed air-water between them. Fourar and Borries (1995) did similar experiments using smooth glass plates and clay bricks. Both studies observed flow structures like bubble, annular and fingering bubbles

comparable to flow in pipes and depicted flow in fractures to be better correlated using the equivalent homogeneous single-phase model. Pan et al. (1996) observed the identical flow structures in their experiment with oil-water systems. They observed that a discontinuous phase can flow as discrete units along with the other phase. Pan et al. (1996) also found their experimental pressure drop to be better predicted by homogenous single-phase model. All of these experiments show significant phase interference at intermediate saturations.

Pruess and Tsang (1990) conducted numerical simulation for flow through rough-walled fractures. They modeled fractures as two dimensional porous media with apertures varying with position. Their study shows the sum of the relative permeabilities is less than 1, residual saturation of the nonwetting phase is large and phase interference is greatly dependent on the presence or absence of spatial correlation of aperture in the direction of flow. Persoff et al. (1991) did experiments on gas and water flow through rough-walled fractures using transparent casts of natural fractured rocks. The experiment showed strong phase interference similar to the flow in porous media. The relative permeability data of Persoff (1991) and Persoff and Pruess (1995) for flow through rough-walled fractures were compared in Horne et al. (2000) against commonly used relative permeability relations for porous media, the X-curve and Corey curve as shown in Figure 1.1.

In both experiments of Persoff (1991) and Persoff and Pruess (1995), flow of a phase is characterized by having a localized continuous flow path that is undergoing blocking and unblocking by the other phase. A recent parallel plate experiment by Su et al. (1999) illustrates the same flow mechanism of intermittent localized fluid flow. Kneafsy and Pruess (1998) observed similar intermittent flow in their experiments with pentane through various parallel plate models made from glass, sandblasted glass or transparent fracture replicas. These observations are contrary to the findings of Fourar et al. (1993), Fourar and Bories (1995), and Pan et al. (1996).

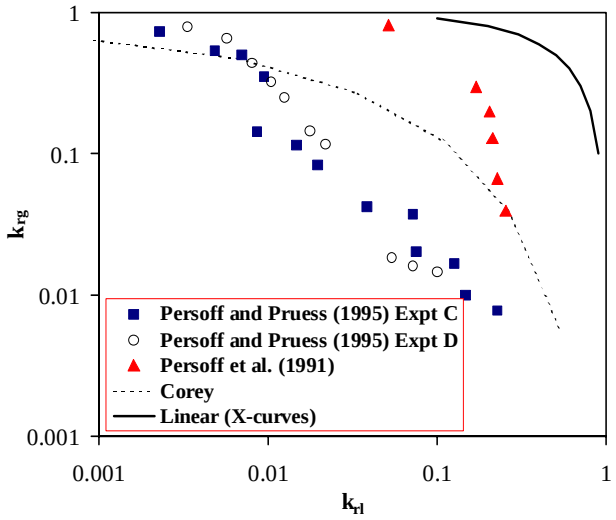

Figure 1.1 Measurement of air-water relative permeabilities in rough-walled fractures (graph from Horne et al. 2000).

Presently, the mechanism of flow and the characteristic behavior of relative permeability in fractures are still undetermined. Issues such as whether a discontinuous phase can travel as discrete units carried along by another phase or will be trapped as residual saturation as in porous medium are unresolved. The question of phase interference, i.e. is the relative permeability curve against saturation an X-curve, Corey or some other function, is still unanswered. The main objective of this study is to contribute to the resolution of these issues.

1.2 EXPERIMENTAL METHODOLOGY

This study consisted of experiments in smooth- and rough-walled fractures. The smooth-walled fracture experiment was done by flowing nitrogen and water in between glass and aluminum plates. The rough-walled fracture experiment was done with nitrogen-water flowing through a wire mesh inserted in between glass and aluminum. The nitrogen-water system was chosen mainly because of its simplicity since it can be done at room temperature and volume changes due to compressibility and solubility are negligible. The system does not have the complication of phase change. The nitrogen-water experiments will aid in establishing a reliable methodology for future study of flow characterization and permeability calculation for more complex systems such as steam-water flow.

Fracture Apparatus Description

The fracture apparatus consists of a smooth glass plate on top of an aluminum plate. The whole apparatus is confined by another metal frame bolted to the bottom plate. This was done to improve the seal and to prevent deformation of the glass due to system pressure. The metal frame has several windows and a mirror attached to it for flow visualization. (See Figure 1.2 and Figure 1.3)

An o-ring (Viton 1/8" thick #2-272) was placed in between the glass and aluminum plates as a seal (see orange color lining in Figure 1.3). Placing this o-ring in the channel is not enough to provide a good seal because the channel was custom made in width and length. Thinly cut rubber sheets were placed at the outer boundary to push the o-ring to the sides of the aluminum plate. These provided an excellent seal when compressed with the glass and metal frame. Since the o-ring is cylindrical in shape and the aluminum plate is rectangular, there will be a narrow channel in between the o-ring and the plate when squeezed together. A thin lining of copper based adhesive (Permatex Ultra Copper) was applied to minimize this channel. It is important to eliminate this channel for it serves as an easy conduit for the fluid to pass through instead of the fracture. The phases enter the fracture through two separate canals. Each canal has several ports drilled in a way that they align on the surface (see Figure 1.2). The surface of the fracture apparatus was designed such that there is a 12” by 4” space available for flow. Throughout this flow area, tiny temperature ports the size of needles were drilled. Needle-size ports were drilled so as to minimize surface discontinuity. A pressure port was drilled at each end of the flow path. The two-phase fluid exits through a single outlet.

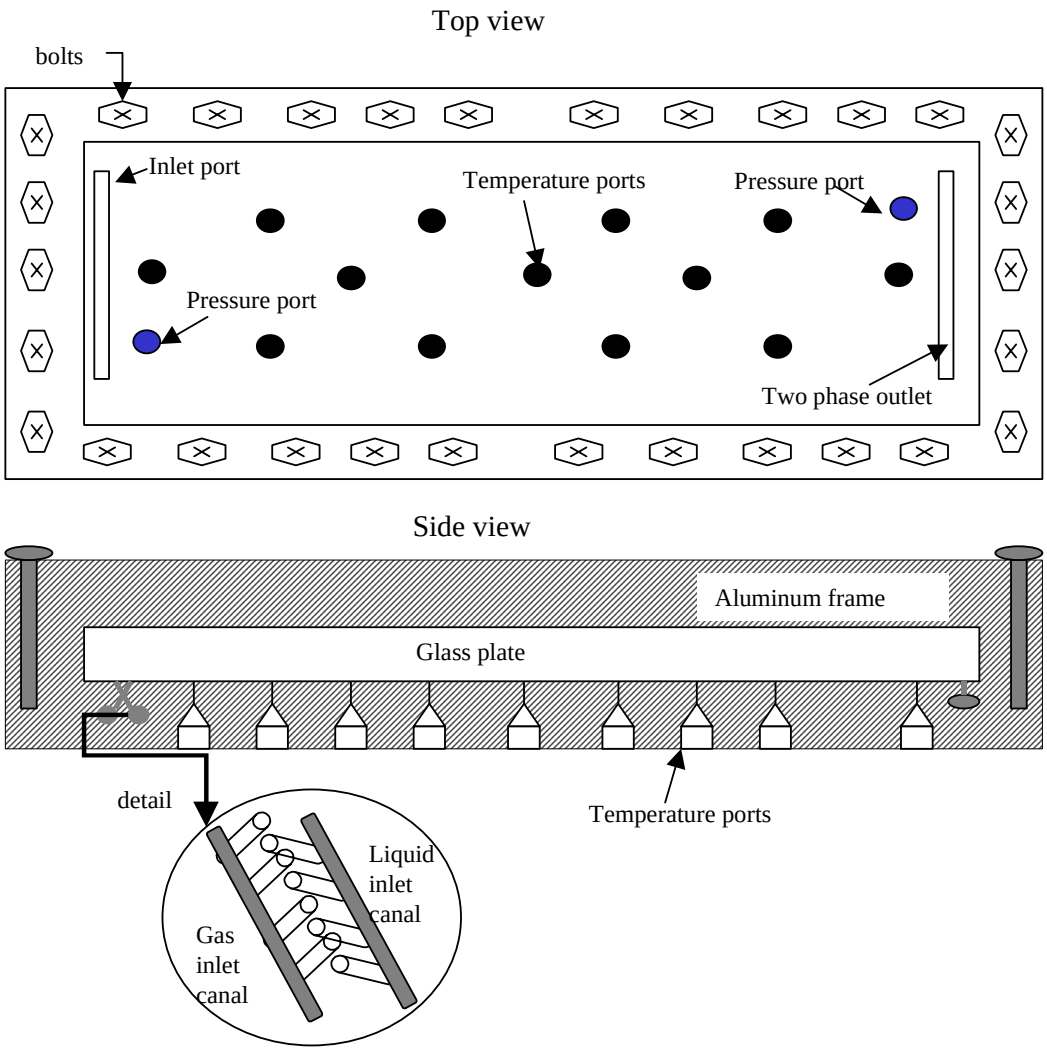

Figure 1.2 Schematic diagram of fracture apparatus.

Figure 1.3 Picture of fracture apparatus.

Control and Measurement Techniques

There are two canals available for input of gas and liquid. The options to input nitrogen and water as separate streams or as mixed fluid in a single stream were tried. It was found that mixing the gas and water prior to input caused no significant improvement in fluid distribution. Thus, the gas and water streams were injected separately for simplicity, ease of flow rate control and inlet pressure reading.

Gas injection was controlled through a flow regulator (Matheson Flow Controller Model 8270). The gas regulator is connected to a gas meter (Matheson Flow Meter model 8170) that gives out a digital display. For water, a meter pump (Constameter pump model III) controls the rate of injection. Distilled deaerated water was used as injection fluid. Red dye was dissolved in the water for better phase identification.

Nitrogen and water enters at the far left of the apparatus. Both phases flow in between the glass and aluminum plate and exit at the far right through a single channel. Attached to the exit is a cross of larger diameter that enables the separation of the phases for outlet pressure measurement. Figure 1.4 is a schematic diagram of this configuration.

Low capacity differential transducers were used to measure the gas phase pressure drop, liquid phase pressure drop and the gas-phase outlet pressure. The liquid differential transducer (Celesco Transducer Model CD 10D range 0-5psi) is attached to the input water stream and to the bottom of the cross separating the phases at the outlet. The gas differential transducer (Celesco Transducer Model CD 10 D range 0-5psi) is connected to the nitrogen inlet and to the top of the cross separator. Another gas transducer (Celesco Transducer Model CD 10D range 0-0.5psi) is attached to the top of the cross separator. This last transducer measures the outlet pressure of the gas. These transducers send electrical signals to a Labview program designed to record pressure data at user specified time interval. See Figure 1.4.

Experience showed that these fracture experiments are unsteady state by nature. At a single gas-water input ratio, there are significant pressure fluctuations accompanied by saturation changes and change in gas flow rate. The water flow rate is considered constant since it is injected by meter pump. Due to this unsteady nature, data acquisition then requires gathering of instantaneous pressure, flow rate and saturation data.

Instantaneous data gathering was accomplished by the use of a digital video camera. Video shots were taken of the pressure, flow rate and saturation data displayed all at the same time. The pressure data were displayed by voltmeters attached to each transducer outlet. The digital output of the gas meter displays the gas flow rate. The saturation was taken from the image of the whole flow area of the fracture. Still images were then taken from the recorded video film. The data gathered from the video was connected with the Labview data through the time read from a digital clock recorded along with the other data. Figure 1.5 shows a typical video image taken from the experiments. See also Figure 1.4.

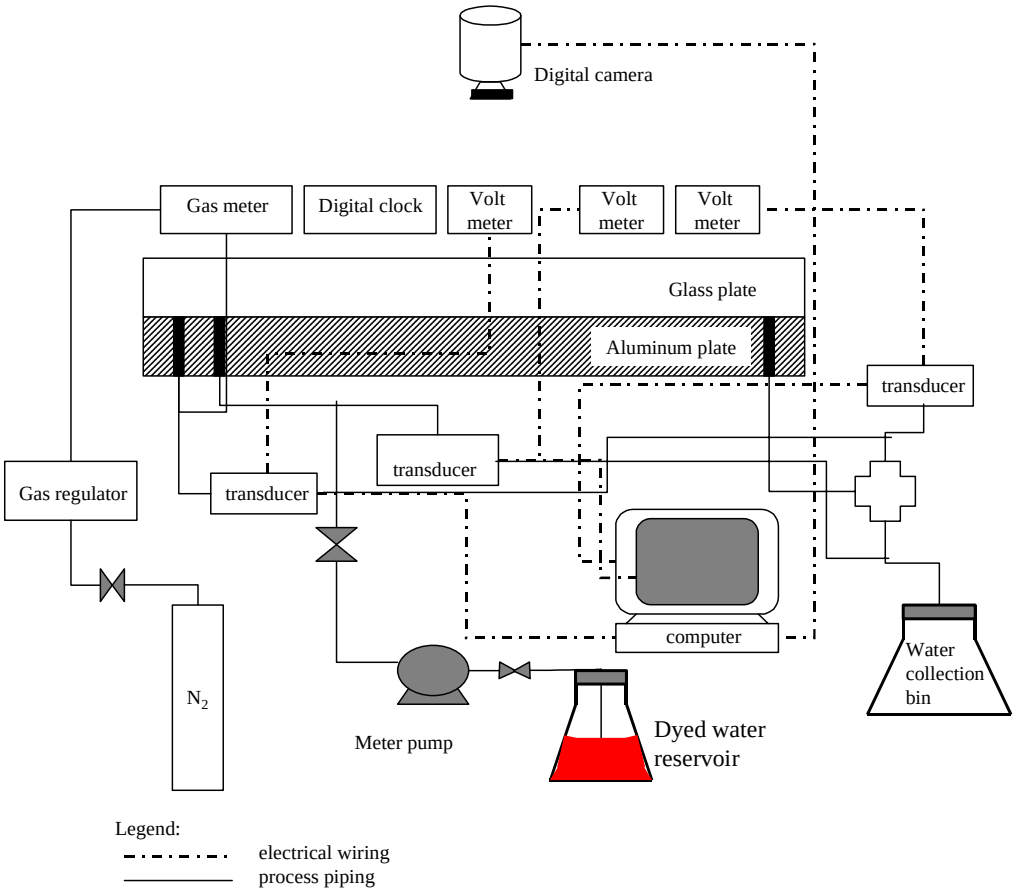

Figure 1.4 Process flow diagram for nitrogen-water experiment.

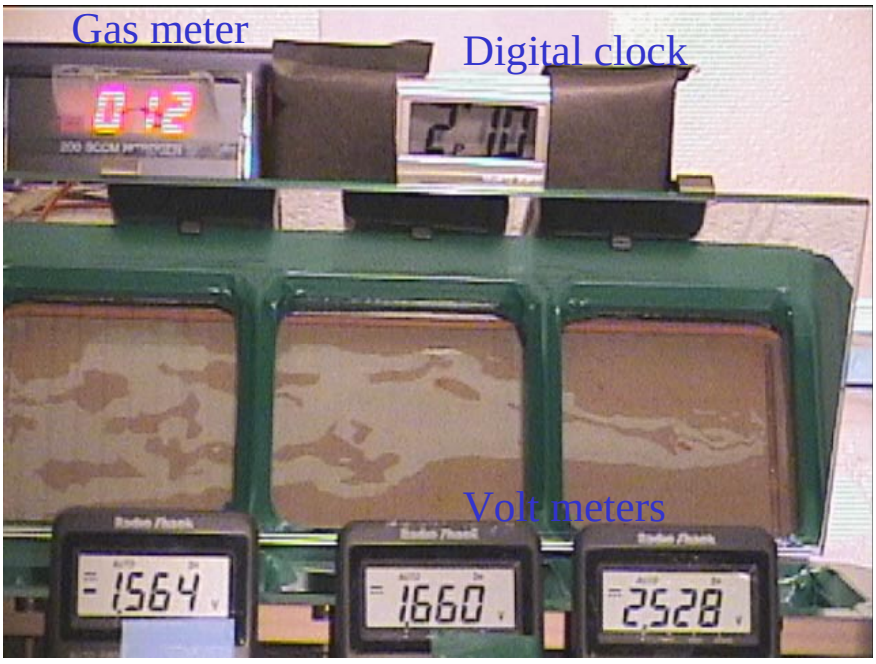

Figure 1.5 Sample video image taken for nitrogen-water runs.

Drainage and imbibition experiments were done for smooth- and for rough-walled fractures. The glass against the aluminum plate represented the smooth-walled fracture while the rough-walled was achieved by inserting a wire mesh between the glass and aluminum plate. The wire mesh is made from 0.00065" (0.0026cm) diameter stainless steel wire and has 30x30 mesh size. For both the rough- and smooth-walled fracture configurations, stainless steel shims were inserted at the perimeter of the flow area in between the glass and aluminum plate. The shims are 0.003" (0.0076cm) thick.

Drainage experiments were performed first. To start, the fracture was fully saturated with water. Unlike in porous media, parallel plates can be easily saturated with water if the aperture is small enough. Full saturation is achieved simply by flowing water at a slow rate into the completely dried apparatus. This approach was used for both the smooth- and rough-walled configurations. The drainage experiment proceeded with the water injected at a constant rate and gas rate increased incrementally. If saturation change was not evident, then both the gas and the water rate were changed. The reverse was done for imbibition. At a specific gas-water ratio, the experiment was made to run for several minutes (usually 30 minutes) or up to a time when the pressure change was minimal or when pressure fluctuations seemed to be in a certain range before taking a video record.

Saturation Measurement

From the still image of the fracture flow shown in Figure 1.5, saturation was computed by measuring the area that each phase occupied. The photographs were processed in a Matlab program. The program first cuts the photograph to display just the image of the flow area. Using this cut image, the program does quadratic discriminant analysis to group the pixels of the picture into three groups: the water phase, gas phase and the frame. The grouping is based on color differences. Saturation is calculated as total pixels of liquid group over the sum of the gas and liquid group. Figure 1.6 is a comparison of the gray scaled image produced by the program and the original cut photograph from the digital camera. The accuracy of the program in calculating the saturation can be related to the similarity in details of the gray scale image to the true image. From the figure, it can be said that the program has reasonable accuracy.

Pan et al. (1996) also used this technique for measurement of saturation. Their study noted that the sources of error in this technique were the quality of the photographs and the water film adsorbed on the surfaces of the plates with the latter being of minimal effect. Good quality photographs are the ones with clear distinction between the gas and liquid phase. The use of dyed liquid enhanced visualization of phase boundaries. Good lighting is also necessary so that the colors in the image come out clearly. The lighting should also be positioned in a way that it does not produce a shadow on the flow area. The program will mistakenly take the shadow as liquid phase even if there is gas. The light should be not too bright or focused too directly on the image to prevent reflection. Reflection will cast a white background on the picture. This will be taken automatically by the program as gaseous phase. In the experiment, good lighting was obtained by taking the picture in the dark with lamps directed on the white ceiling to create adequate lighting on the apparatus.

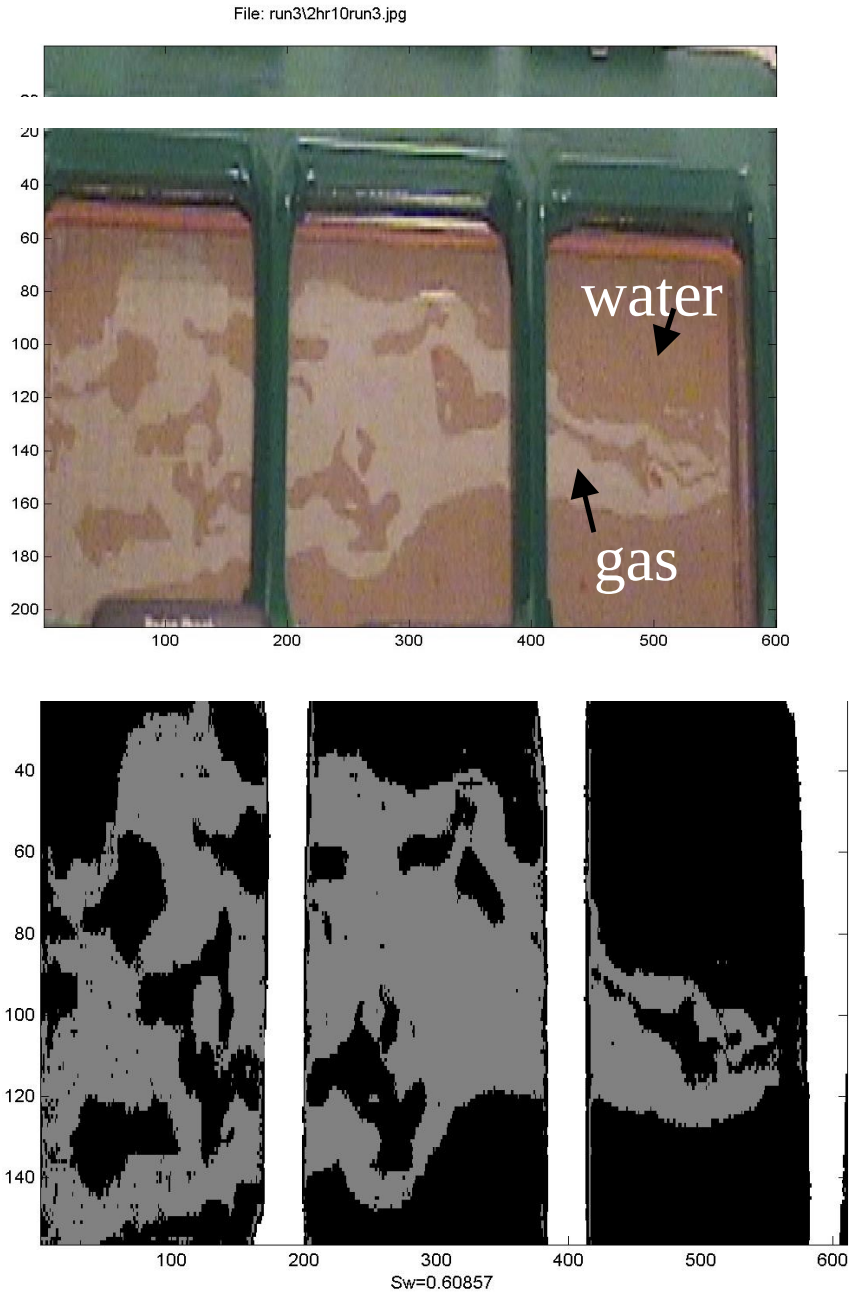

Figure 1.6 Comparison between the true color image of the fracture flow and gray scale image from Matlab program used in measuring saturation.

1.3 RESULTS AND DISCUSSION

Smooth-walled Fracture Experiments

Observed Flow Mechanism

One dominant flow mechanism was observed in the smooth-walled fracture experiment. Each phase travels through the fracture by forming a localized continuous flow path. This flow path is unstable as the other phase constantly blocks and unblocks certain points in the path.

For example in the drainage experiment, the gas forms its own flow path through the liquid-dominated fracture. This flow path undergoes continuous snapping and reforming due to the invasion of water. This blocking and unblocking of flow path causes continuous pressure fluctuations throughout the experiment even at a constant gas-water ratio. Figure 1.7 shows the pressure fluctuations and the corresponding events observed. Snap shot images of the flow at these times are seen in Figure 1.8. These pictures were taken at a gas rate of 19 cc/min and water rate of 8.5 cc/min. It was observed that the lower pressure drop corresponds to the time when gas is establishing its channel (see time 2:14 p.m. in Figure 1.7 and Figure 1.8). Upon establishing a complete path, gas is able to rush through the fracture length. This causes an increase in the gas pressure drop. As the gas surges, there is more space for water to come through the fracture. Water invades the gas channel (see time 2:16 p.m. in Figure 1.7 and Figure 1.8). As water breaks through there is an increase in liquid phase pressure drop. These are the pressure peaks seen in Figure 1.7. The cycle continues with the gas forming its pathway and water invading it (see time 2:17 p.m. and 2:18 p.m. in Figure 1.7 and Figure 1.8).

This flow mechanism of moving through a continuous flow path was observed over a wide range of gas-water ratios from 10^{-1} to 10^{4}. The width of the flow path increases as gas rate increases. This flow path, however, was continuously being broken up by the water phase and reforming again. Figure 1.9 illustrates some examples.

This flow mechanism shows the unsteady nature of the experiment. Even at constant gas and liquid injection rate, pressure fluctuates and saturation changes as fracture space change from being a gas path to water path and vice versa. This emphasizes the importance of acquiring instantaneous pressure, saturation and flow rate measurements.

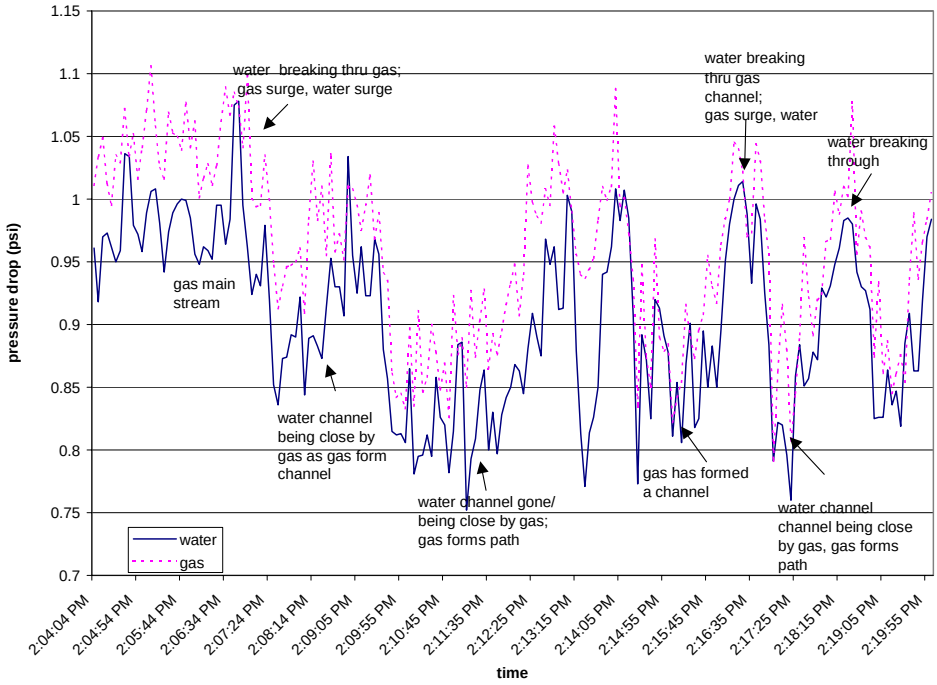

Figure 1.7 Pressure fluctuations caused by the breaking and reforming of gas flow path.

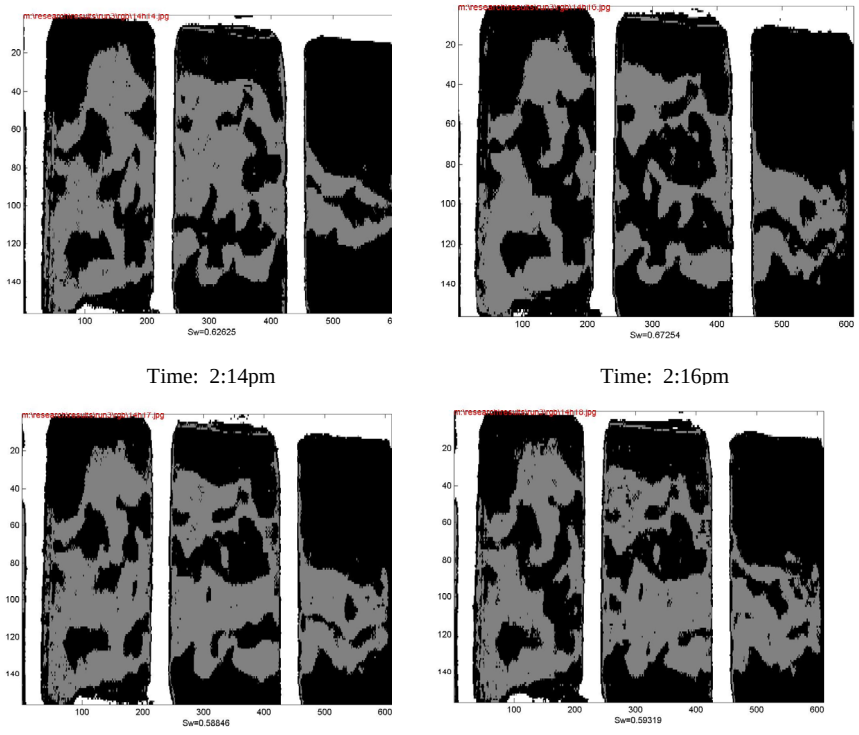

Time: 2:14pm Time: 2:16pm

Time: 2:17pm Time: 2:18pm

Figure 1.8 Images showing the forming and breaking of the gas flow path corresponding to the time in Figure 1.7.

Gas rate: 0.5 cc/min water rate 8.5 cc/min

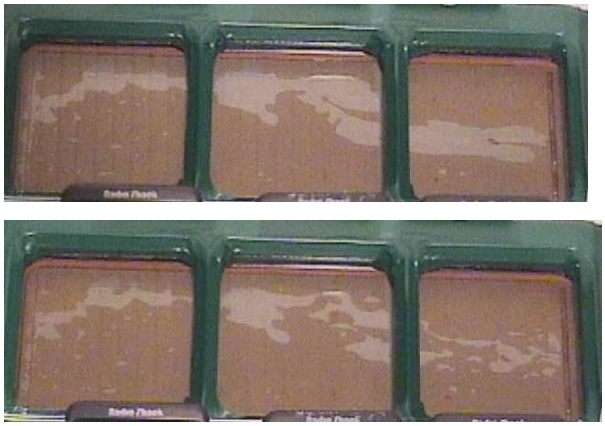

Gas rate: 19 cc/min water rate 8.5 cc/min

Gas rate: 140 cc/min water rate 8.5 cc/min

Figure 1.9 Examples of gas flow path increase in width as gas flow rate increases and water breaking up this flow path.

Persoff and Pruess (1995) observed a similar flow mechanism in their experiment with air-water flow in a transparent fracture replica. They also related the pressure fluctuations with the blocking and unblocking of flow path. They modeled the behavior as flow through a cylindrical tube of constant radius with a certain critical throat point of radius very much smaller than the tube. Through their model they were able to prove that a phase flow path in fractures will be unstable and will consequently be invaded by the other phase. This observation is also consistent with the findings by Su et al. (1999), Kneafsy and Pruess (1998) and numerical simulation by Pruess and Tsang (1990) where the flow mechanism was described as intermittent localized flow.

Intermittent localized flow observation is contrary to that of the concept of moving "islands" or flow structures carried by one phase as observed by Fourar and Bories (1995), Fourar et al. (1993), and Pan et al. (1996). The superficial velocities for the smooth-walled experiment are graphed on Fourar and Bories (1995) flow pattern map in Figure 1.10. Although, the data covered a wide range of the proposed flow patterns, these flow patterns were not seen in the experiment here. The intermittent localized flow observed is more comparable to flow in porous media. Phases in the experiment move only through continuous phase paths like in porous media. But unlike porous media, the phase paths or occupancy are not constant but are rapidly changing and reforming.

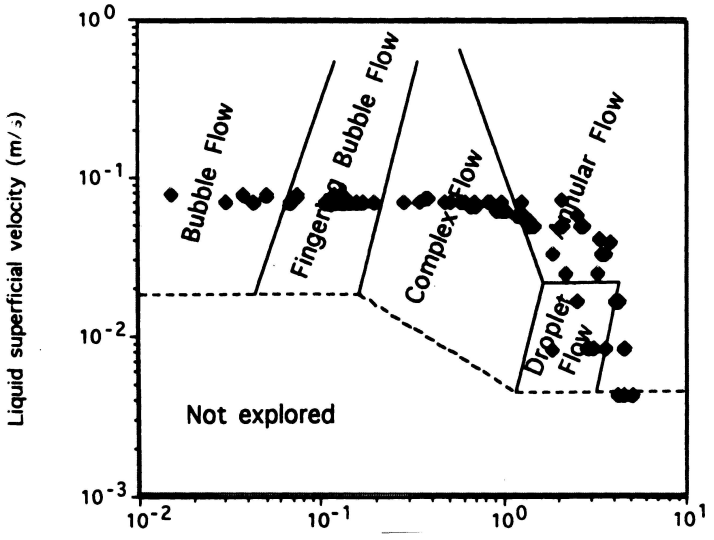

Figure 1.10 Smooth-walled fracture experimental velocity data imposed in Fourar and Bories (1995) flow map for glass channel.

Relative Permeability Curve From Porous Medium Approach

Eqn. (1.4) and Eqn. (1.5) for Darcy flow of two-phase flow were used to calculate relative permeabilities. The use of these equations requires the knowledge of the fracture

absolute permeability. The absolute permeability was derived using Eqn. (1.1) with the pressure drop and flow rate coming from single-phase liquid experiments.

Two single-phase experiments were done. The results of these are illustrated in Figure 1.11. Run #1 was done in sequence with the smooth-walled experiments. After noticing that the absolute permeability changes with flow rate, Run #2 was done several weeks later with a different pump to investigate a wider flow rate range. Both runs show that for pressures below 0.5 psi, k_{abs} is changing with flow rate. This implies that the fluid is lifting the glass as it flows through the fracture. At pressures greater than 0.5psi, the glass is lifted to its maximum height defined by the confinement of the metal frame. At this pressure range, the absolute permeability is constant. All the data points in the experiment lie in this range of constant absolute permeability (see Appendix B). However, the results of the two experiments were conflicting in terms of magnitude. The choice of which absolute permeability to use will affect the magnitude of the calculated relative permeability but will not affect the shape of the relative permeability curve. The highest absolute permeability derived from Run #1 was used.

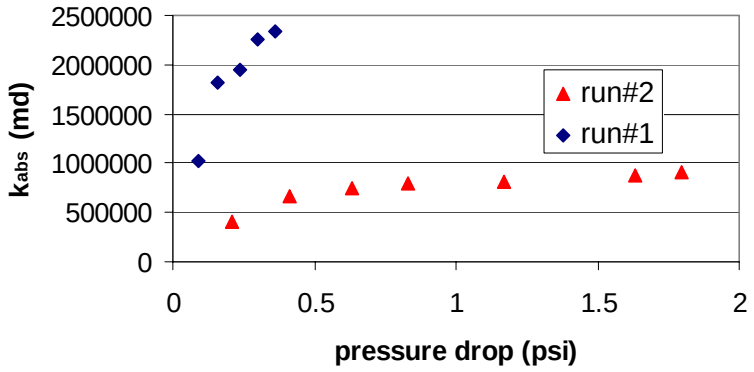

Figure 1.11 Absolute fracture permeability derived form single-phase liquid experiments for smooth-walled fracture

The results are graphed in Figure 1.12. In this figure, neglecting the data enclosed in the square boxes, the relative permeability curve has the shape of Corey curve (Corey, 1954). This follows with the observation that the flow in the smooth-walled fracture is comparable to flow in porous media. It is also noticeable that the sum of the relative permeabilities at a particular saturation is less than unity. This indicates phase interference. This is consistent with the observed flow mechanism where the gas and water compete in establishing pathways through the fracture.

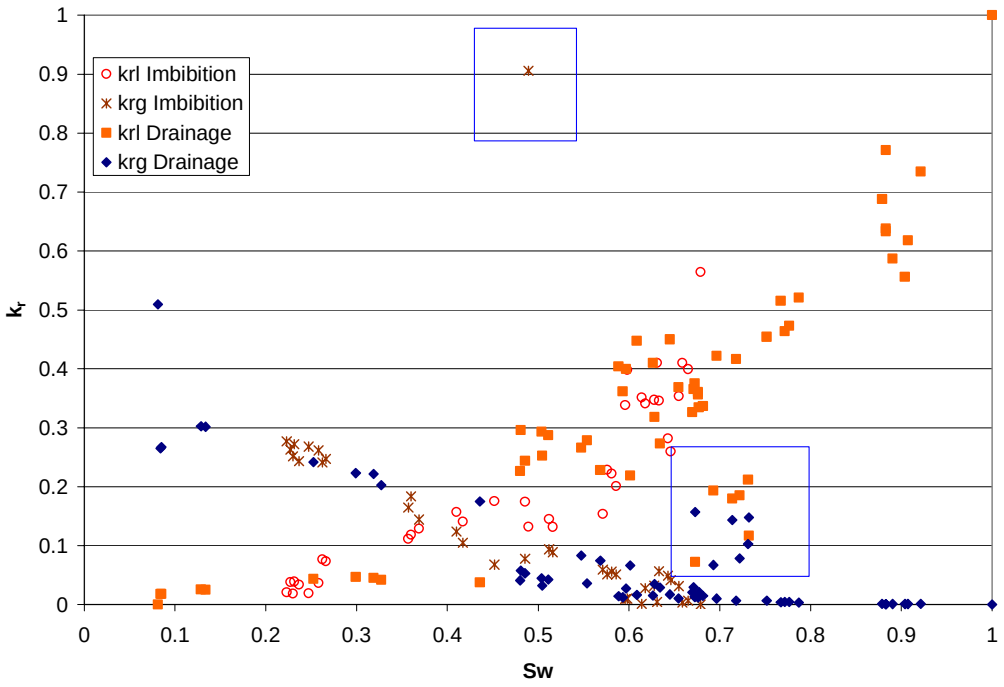

Figure 1.12 Relative permeability data obtained from smooth-walled fracture experiment

The data for both imbibition and drainage experiments were fitted separately with the Honarpour et al. (1982) expression:

$$k_{rw} = k_{rwo}\left[\frac{(S_w - S_{wr})}{(1 - S_{wr} - S_{gr})}\right]^{n_w} \tag{1.18}$$

$$k_{rg} = k_{rgo}\left[\frac{(1 - S_w - S_{gr})}{(1 - S_{wr} - S_{gr})}\right]^{n_g} \tag{1.19}$$

with

$$k_{rwo} = k_{rw}(S_{wi}) \tag{1.20}$$

$$k_{rgo} = k_{rg}(S_{wr}) \tag{1.21}$$

S_{wi} being the initial water saturation for drainage while for imbibition

$$k_{rwo} = k_{rw}(S_{gr}) \tag{1.22}$$

$$k_{rgo} = k_{rg}(S_{wi}) \tag{1.23}$$

The resulting curves are graphed in Figure 1.13 and Figure 1.14. The parameters for the fitted curved are tallied in Table 1.1. In both graphs, the fitted Honarpour curves give good representation of the trend of relative permeability data with saturation. The fitted curves have different exponents for the Honarpour expression for imbibition and drainage. This is even though the data for both drainage and imbibition seem to lie in same trend as seen in Figure 1.12. This shows the effect of saturation history on relative permeability. Compared to the Corey expression from Eqn. (1.9) and (1.10), the drainage

experiments have dissimilar exponents. For imbibition, however, the value of n_w (4.57) and n_g (1.92) are close to Corey exponents of 4 for n_w and 2 for n_g.

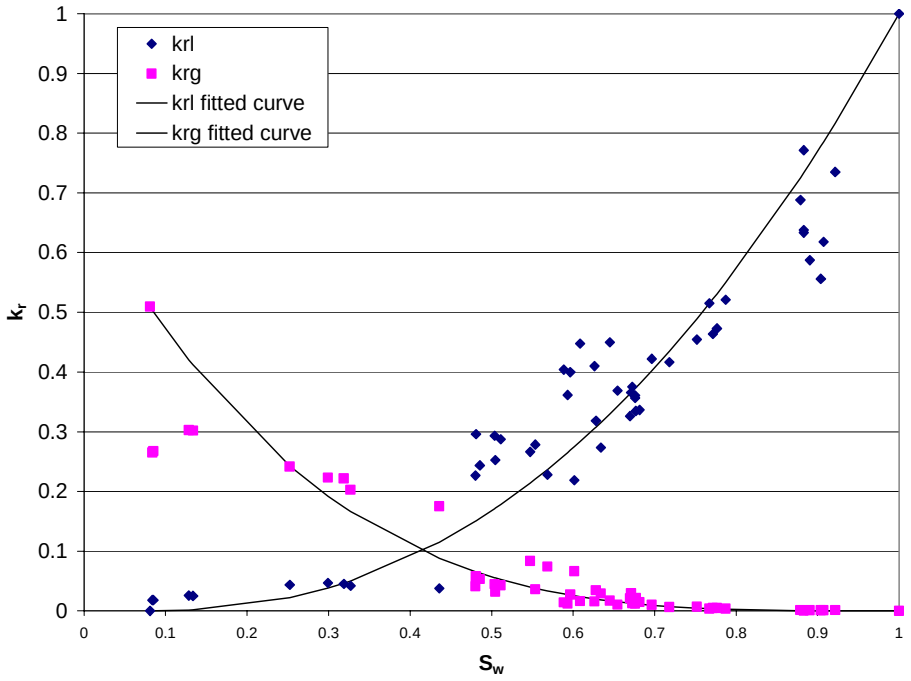

Figure 1.13 Fitted Honarpour expression for smooth-walled fracture drainage experiment.

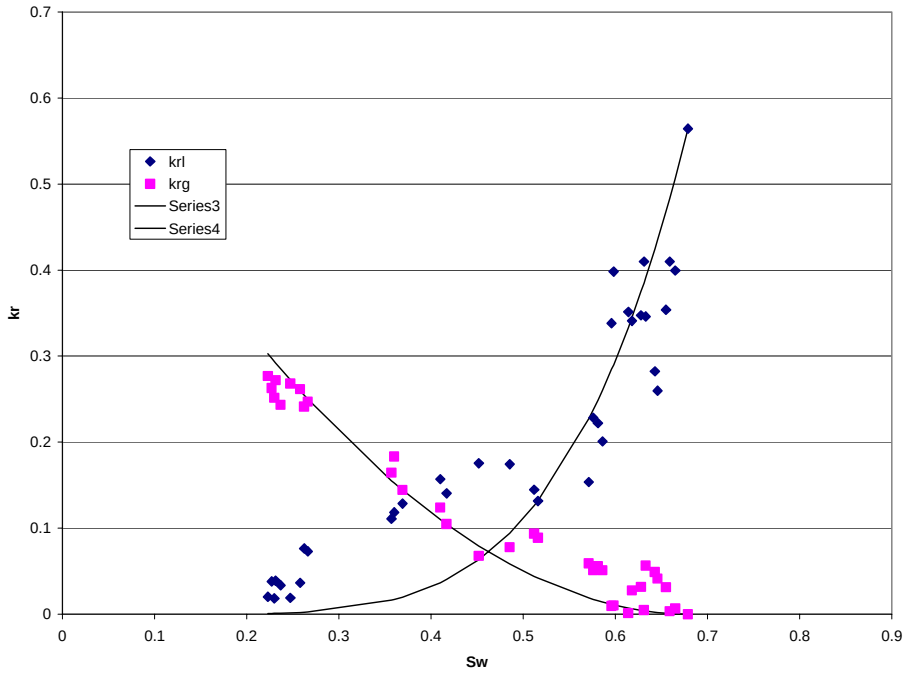

Figure 1.14 Fitted Honarpour expression for smooth-walled fracture imbibition experiment.

Table 1.1 Fit Parameters for smooth-walled fracture experiment

	Drainage	Imbibition
Swr	0.081	0.081
Sgr	0	0.321
krwo	1	0.564
krgo	0.509	0.509
nw	2.27	4.57
ng	3.59	1.92

Application of Homogeneous Single-Phase Pipe Flow Model for Smooth-walled Fracture

The homogeneous single-phase pipe flow model was also applied in the data for the smooth-walled fracture. The table of calculation for this model is included in Appendix B. Figure 1.15 depicts the calculated friction factor with the modified Reynold's number in a log-log chart. From the fitted linear equation, the constants *C* and *n* in Eqn. (1.17) are 3.23 and 0.75 respectively. Figure 1.16 compares this result to previous works for parallel plate experiments. The slope of the fitted line (-0.75) is lower than the usual finding of negative unit slope for laminar flow. Among all the studies, the data is closer to Romm (1966).

The fit of Eqn. (1.17) for friction factor as a function of Reynold's number with the experimental data is not so good. Thus, pressure drop calculated from Eqn. (1.12) inadequately predicts the experimental data (see Figure 1.17). This was expected since the observed flow mechanism was not similar to flow regimes in pipes on which this model is based.

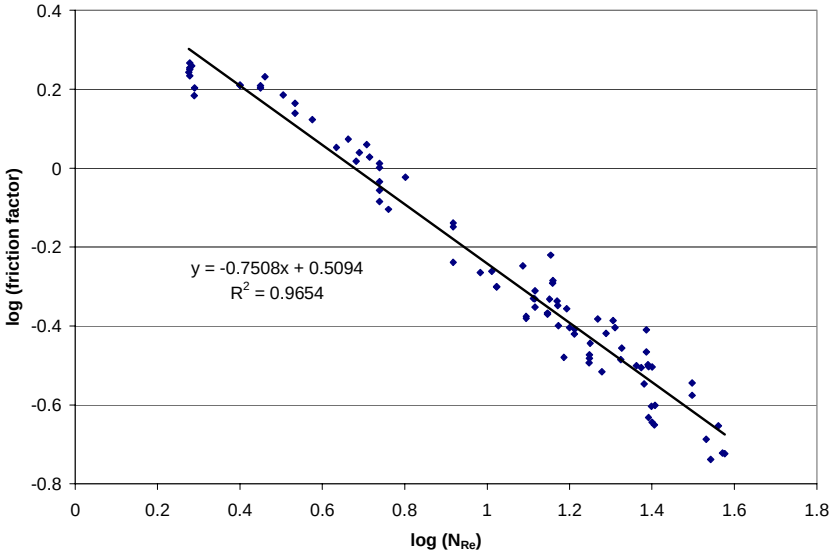

Figure 1.15 Natural logarithm of friction factor with natural logarithm of Reynold's number from data of smooth-walled fracture experiment.

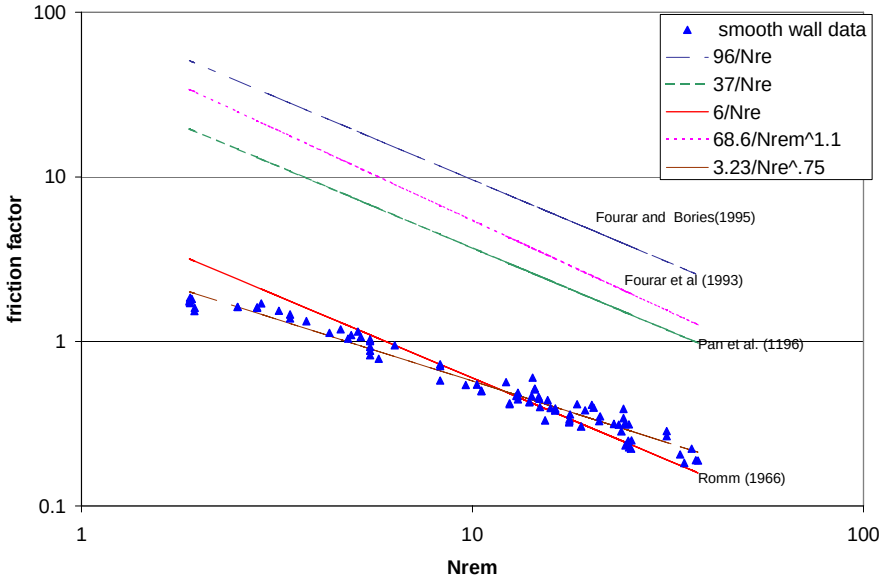

Figure 1.16 Friction factor against modified Reynold's number for smooth-walled fracture in comparison to previous works.

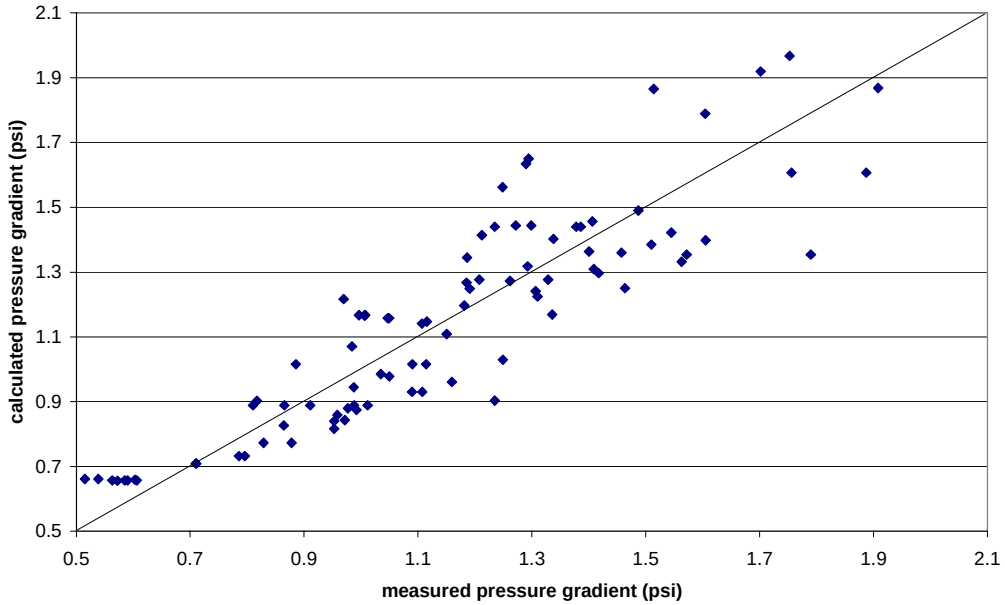

Figure 1.17 Comparison of the predicted pressure drop from homogeneous model and measured data for smooth-walled fracture.

Rough-Walled Fracture Experiments

Observed Flow Mechanism

Similar to the smooth-walled fracture experiments, a phase in the rough-walled fracture experiment during drainage moved by establishing a continuous flow path for itself. However, the stability of the phase path varied greatly with gas-water ratio.

At low gas-water ratio, the gas invades the liquid-dominated fracture and establishes a path (see Figure 1.18). The path built is wider than that in the smooth-walled fracture at the same gas-water ratio. This may be because the mesh gives the gas a way to move horizontally in the fracture even at low gas-water ratio. This path is very unstable. Water quickly invades it almost completely leaving few scattered residual gas areas. The residual gas areas left are not enough to establish a path. Thus, the fracture after the invasion of water can be said to return to its liquid-dominated condition. Within this liquid-dominated condition, the gas will again construct its own flow path and the cycle continues. Figure 1.19 shows two examples of gas flow channels, the water invasion that proceeds it and the residual gas areas left after the water invasion.

The formation of the gas path and the consequent water invasion again goes along with pressure fluctuations. Figure 1.20 shows the pressure data for Figure 1.18 and picture set (A) in Figure 1.19. Similar to the smooth-walled fracture, the low pressure drop corresponds to the forming of the gas path, followed by a peak of both gas and liquid pressure related to the surge of the two fluids through the fracture. It was observed that the magnitude of the pressure peaks decreases as the gas-water ratio increases.

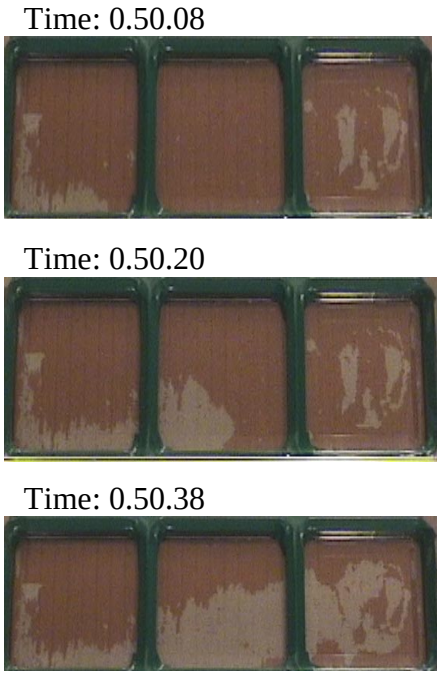

Figure 1.18 Gas invasion in drainage experiment with rough-walled fracture.

The diminishing magnitude of the pressure fluctuations relates to the point when the gas has established a stable path. With a stable path, gas can travel more smoothly and surge flow does not occur. Without surge flow, large pressure fluctuations are not observed. A stable gas path was reached at high gas-water ratio. As in the smooth-walled fracture, the stable gas channels increase in width with increasing gas-water ratio (see Figure 1.21). Within these established gas paths, water sometimes forms narrow channels but these channels are unstable. Water flow is mostly at the edge of the gas path. In the ratios of stable phase paths, saturation can be considered constant at one gas-water injection rate.

For the imbibition experiment, two flow mechanisms were observed. At low gas-water ratio, a stable flow path was seen (see Figure 1.22). This stable flow path is similar to that in the smooth-walled fracture and for the drainage experiment in the rough-walled fracture. At high gas-water ratio (50 and above), a wave-like flow similar to flow in pipe was observed. In this flow, water travels like a wave or a steady front covering the entire fracture. This wave flow caused an increase in the pressure drop exceeding the maximum of the pressure transducer. Thus, the magnitude of the pressure drop when a wave front occurs can be higher than 5psi. Figure 1.23 shows a sample of wave-like front and its corresponding pressure peaks.

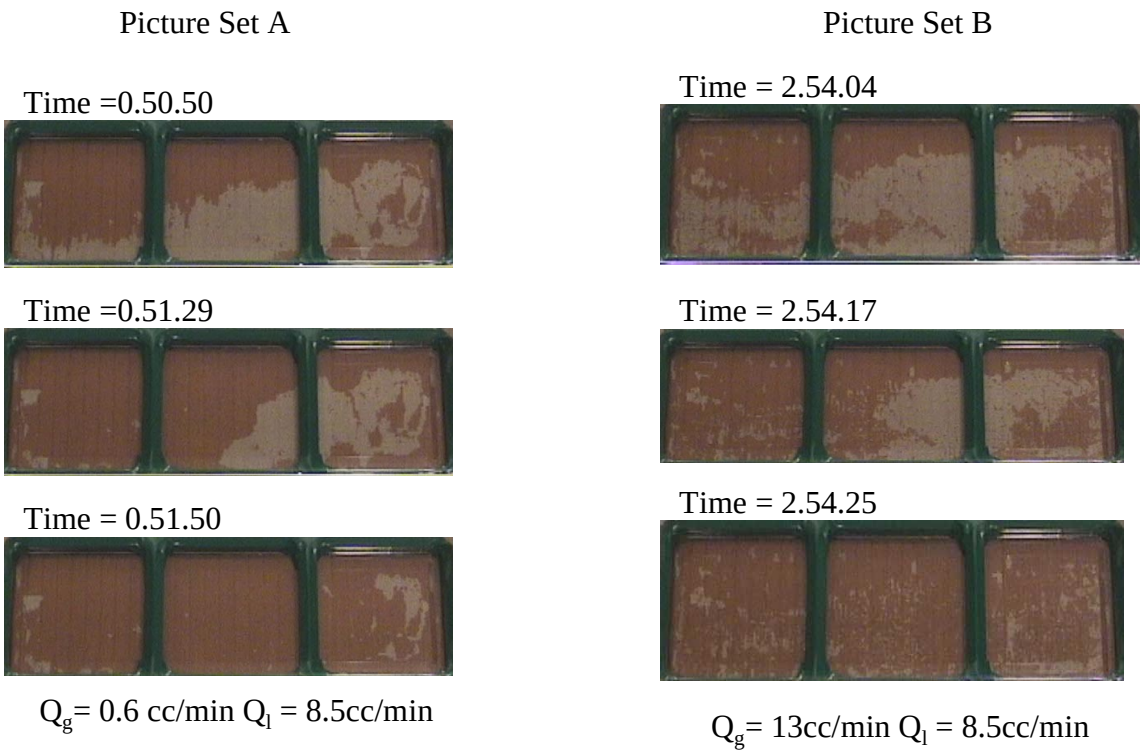

Figure 1.19 Examples of gas flow path, the invasion of water that follows and the residual gases left in rough-walled drainage experiment.

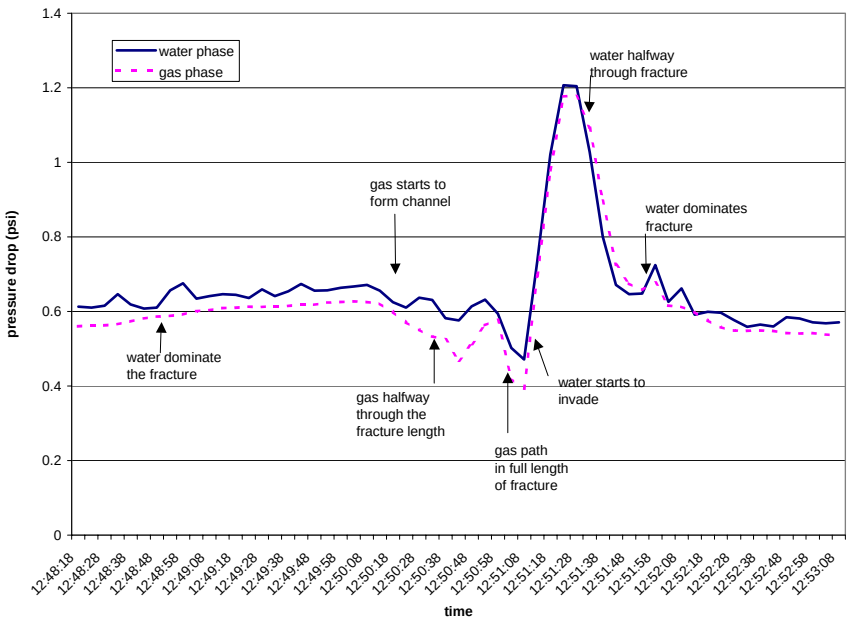

Figure 1.20 Example of pressure fluctuations caused by the building and breaking up of gas and water path. Pictures for this time span are shown in Figure 1.18 and picture set A in Figure 1.19.

Qg/Ql = 5

Qg/Ql = 7.5

Qg/Ql = 17

Qg/Ql = 42

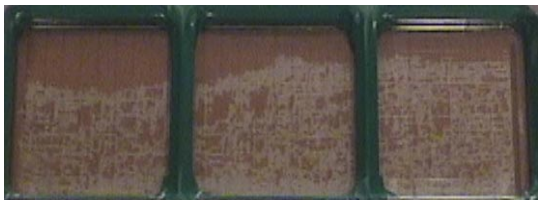

Figure 1.21 Images showing stable gas path in high gas-water ratio for rough-walled fracture.

Q_g = 125 cc/min Q_l = 7.5cc/min

Q_g = 50 cc/min Q_l = 9cc/min

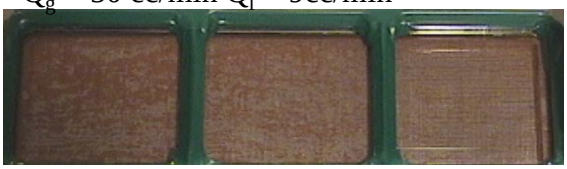

Figure 1.22 Images showing examples of stable flow path of imbibition experiment in the rough-walled fracture.

In all the experiments for the rough-walled fracture, there was considerable amount of trapped phases in the fracture as seen in the red and white isolated spots in pictures from Figure 1.18 to Figure 1.23. This is likely since the mesh provided small corners for the wetting phase to cling to and be trapped in the gas-dominated area of the fracture. It also provided a means to trap the nonwetting gas phase in the small empty space of the mesh as the water surrounds the walls.

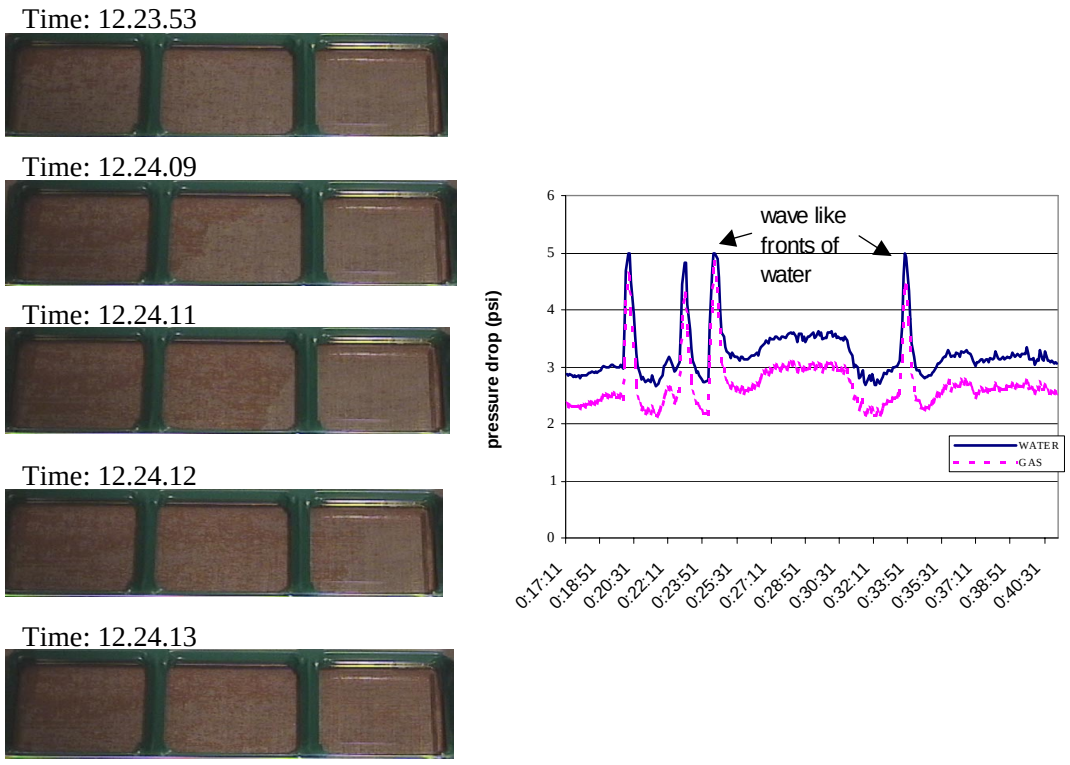

Figure 1.23 Picture of wave-like fronts seen in high gas-water ratio at imbibition experiment and its corresponding pressure peaks.

Relative Permeability Curve Through Porous Medium Approach

The calculation procedure was repeated for the data gathered in the rough-walled fracture experiments.

Several single-phase rough wall experiments were done to determine the absolute permeability of the fracture. The calculated absolute permeabilities from these experiments are shown in

Figure 1.24. The reason for the variation of the absolute permeability value with pressure was discussed earlier. As in the smooth-walled fracture, the absolute permeability remains constant at pressures greater than 0.5 psi. Since all the experiments were at pressures higher than 0.5 psi, absolute permeability was taken as the average of the measurements with pressures greater than 0.5 psi. The absolute permeability value used was 1,950 darcy.

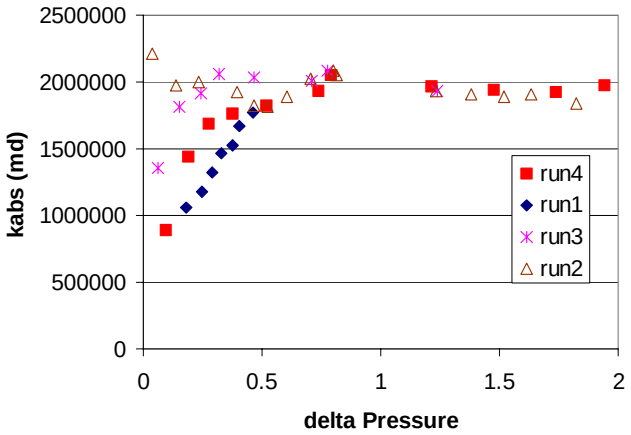

Figure 1.24 Absolute permeability from single-phase experiments for rough-walled fracture model.

Figure 1.25 shows the complete data from the drainage experiment for the rough-walled apparatus. This graph shows the relative permeability taken when the gas path was an unstable surging conduit and when it was a stable channel. Noticing that the flow is more comparable to porous flow when the gas has established a stable path, the data for the unstable gas surge was removed. The remaining data are seen in Figure 1.26. This figure displays a more defined trend. This indicates that the porous medium approach is more applicable to model flow through the rough-walled fracture when flow is characterized by established phase paths. It also suggests that other means of data analysis are needed for the data corresponding to unstable gas surge.

For imbibition, the calculated relative permeability for all types of flow mechanism observed is seen in Figure 1.27. The graph of relative permeability is too scattered showing no obvious relationship. One factor that may have caused this is the uncertainty with regards to saturation measurement for the imbibition experiment of rough-walled fracture. The picture for the imbibition experiment has lower picture quality than the other experiments and saturation analysis was more difficult due to trapped water and gas phase scattered throughout the flow area. Figure 1.28 demonstrate how the programs for saturation measurement were unable to capture the finer details of trapped phases. This effect diminishes as the stable fluid pathway is established with decreasing gas-water ratio.

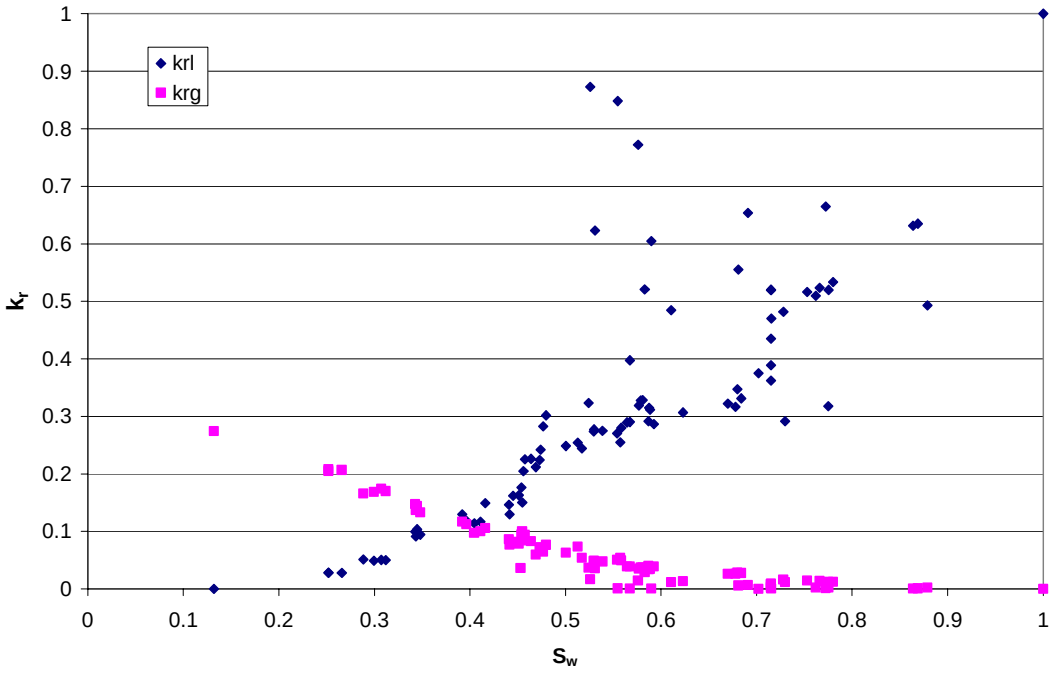

Figure 1.25 Relative permeability data for drainage experiment for rough-walled fracture model.

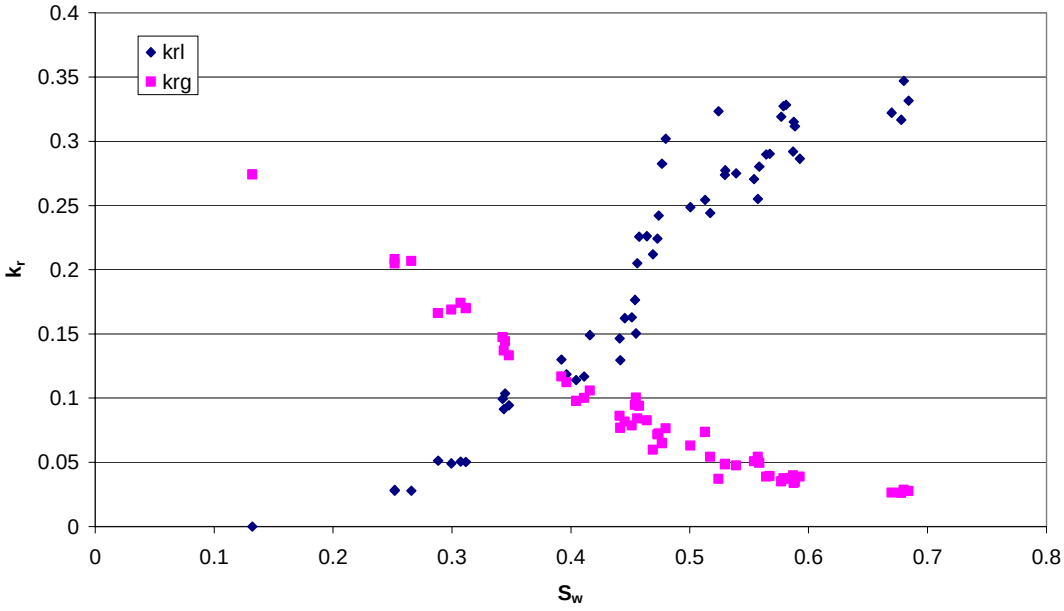

Figure 1.26 Relative permeability data for rough-walled model when the gas path is stable.

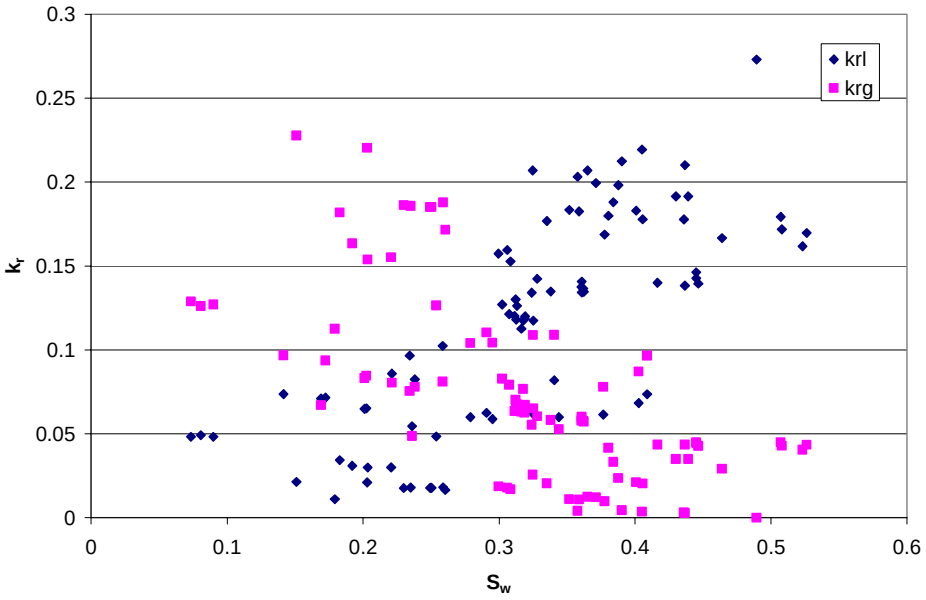

Figure 1.27 Relative permeability data for rough-walled fracture imbibition experiment.

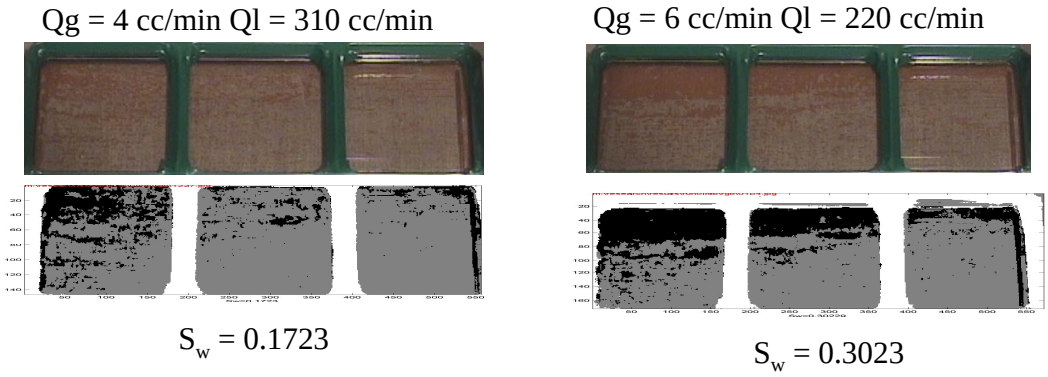

Figure 1.28 Examples of saturation measurement for imbibition experiment with rough-walled fracture.

The data corresponding only to flow characterized by a stable fluid pathway was chosen and graphed in Figure 1.29. Although Figure 1.29 is an improvement over Figure 1.27, the association between relative permeability and saturation is still unclear. These data for imbibition are graphed along with the drainage data in Figure 1.30. This graph shows that relative permeability for the nonwetting phase in imbibition is lower than that of drainage while the opposite is true for the wetting phase. This is consistent with studies for oil-water systems (Amyx et al., 1960) and steam-water systems (Li et al., 1999). Amyx et al. (1960) noted that the imbibition process causes the nonwetting phase (oil) to lose its mobility at high values of wetting phase saturation while the drainage process causes the wetting phase to lose its mobility at higher values of wetting phase saturation.

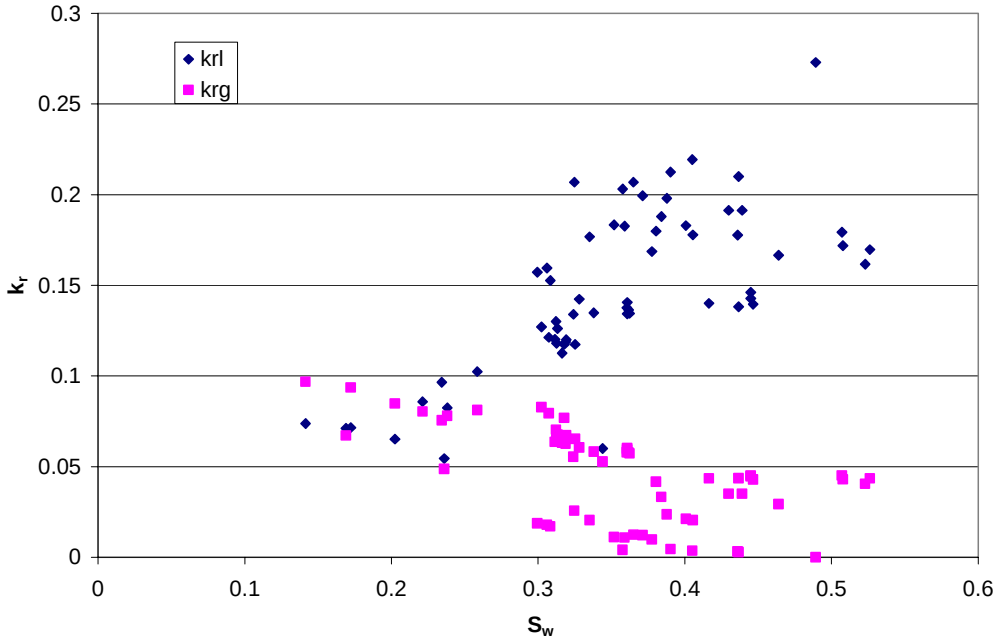

Figure 1.29 Relative permeability for rough-walled imbibition experiment for flow with stable phase path.

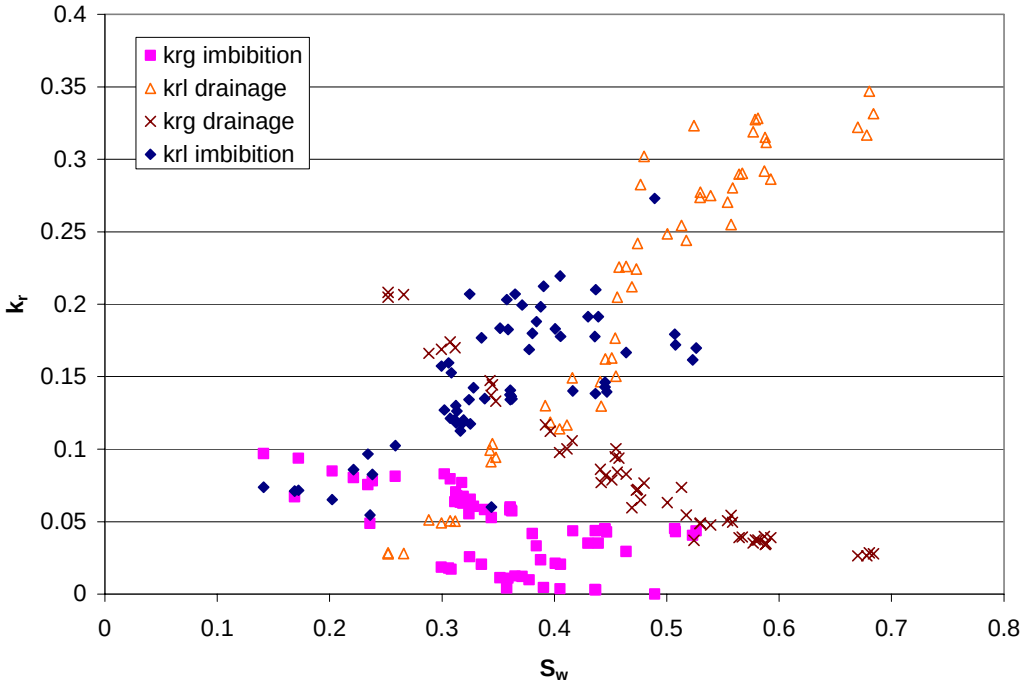

Figure 1.30 Drainage and imbibition data for rough-walled fracture.

The Honarpour relation was fitted to the drainage and imbibition data separately. The resulting fit parameters are tabulated in Table 1.2. As expected, there is a good fit with the drainage data but not with the imbibition data. The exponents of the fitted curves are different for imbibition and drainage and both are far from Corey values.

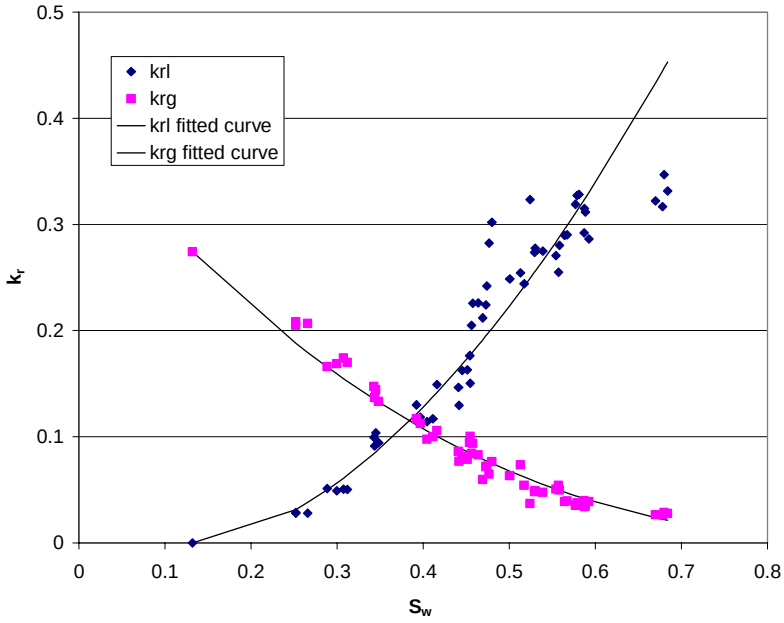

Figure 1.31 Fitted Honarpour curve for drainage data in rough-walled fracture experiment.

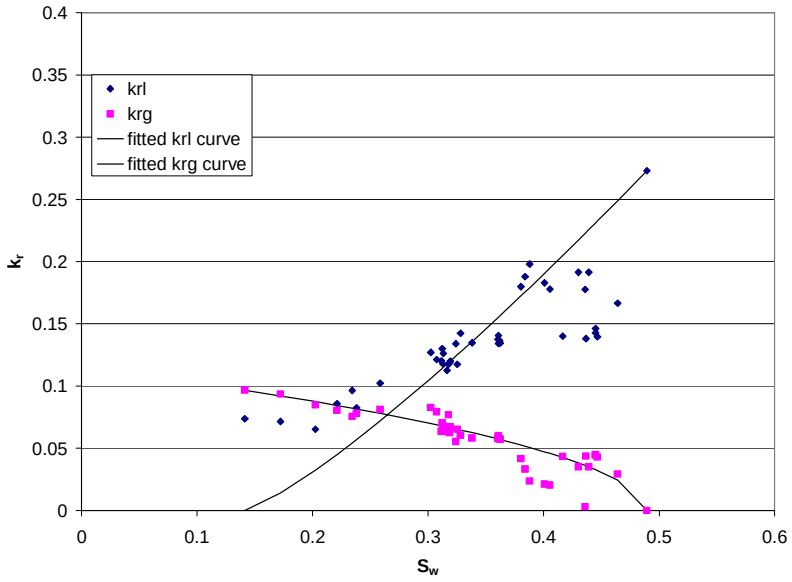

Figure 1.32 Fitted curve for imbibition rough-walled fracture experiment.

Table 1.2 Honarpour fit parameters for rough-walled experiment.

	Drainage	Imbibition
Swr	0.132	0.141
Sgr	0	0.51
krwo	1	0.27
krgo	0.274	0.1
nw	1.75	1.2
ng	2.53	0.52

Application of Homogeneous Model for Rough-Walled Fracture Experiment

It was discovered in the previous section that the porous medium approach when applied only through flow characterized by stable phase paths yields better defined relative permeability curves. This indicates that different flow mechanisms may require different mathematical approaches. Thus in the application of the homogeneous model to the rough-walled fracture experiment, the appropriateness of the model was reviewed for all data and for data corresponding only to unstable surge flow.

The natural logarithm of the calculated friction factor and Reynold's number is seen in Figure 1.33. Graph A includes all the data while graph B consists only of the data corresponding to unstable surge flow. Comparisons of graphs A and B show that removing the stable flow data removed the cluster of data points. The observation that stable flow data tend to cluster in plots of friction factor with Reynold's number suggests that the homogeneous single-phase model is not the appropriate model for this kind of flow. However, considering only the surge data as was done in graph B of Figure 1.33 also did not improve the goodness of fit. For both graphs, there exist some data points that lie vertically with respect to each other. This can indicate either two things that the friction factor may not be a sole function of Reynold's number or that Reynold's number is not a good correlation variable for friction factor in flow through fractures. The calculated friction factor and Reynold's number are compared to other data in Figure 1.34. Again both data sets have slopes lower than unity and the data are closer to Romm's expression (Romm, 1966). The values for the constants C and n are listed in Table 1.3. The pressure drop calculated from these values are compared to measured data in Figure 1.35. Since the fit of the friction factor with the experimental data was not so good, the computed pressure drop from Eqn. (1.12) was not able to satisfactorily predict the experimental pressure gradient.

Table 1.3 Homogeneous equivalent single-phase fit parameters.

Experiment	**C**	**n**
Imbibition rough wall experiment	6.5	-0.83
Drainage for rough wall experiment	2.8	-0.66
Smooth wall experiment	3.23	-0.75

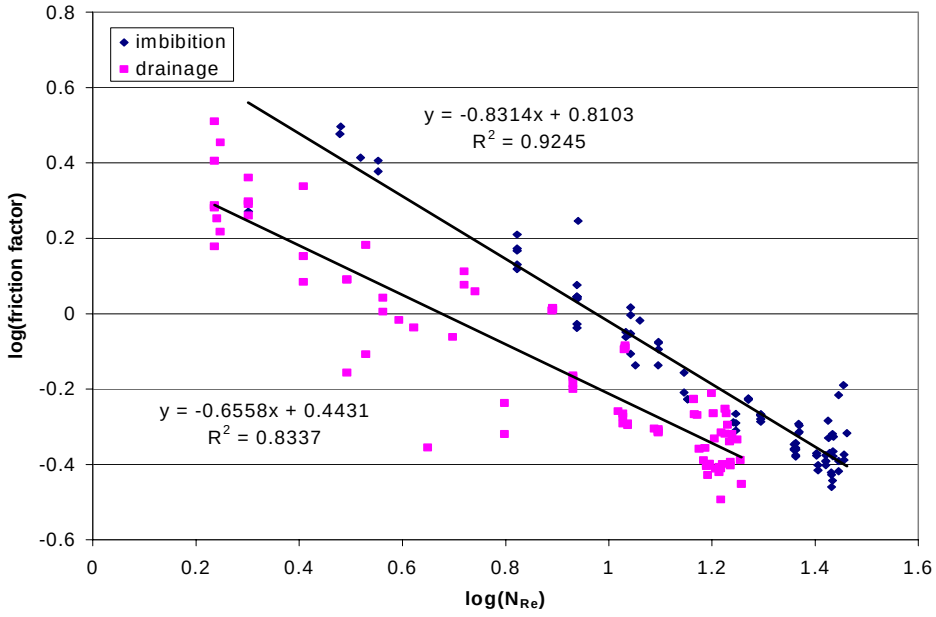

(A)

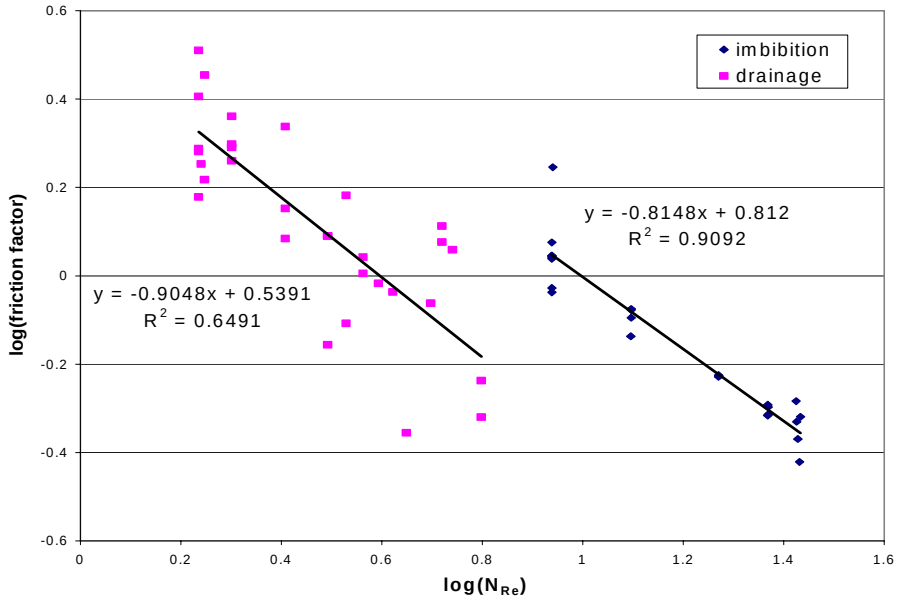

(B)

Figure 1.33 Natural logarithm of friction factor with natural logarithm of Reynold's number for (a) all rough-walled data and (b) for data with unstable surge flow.

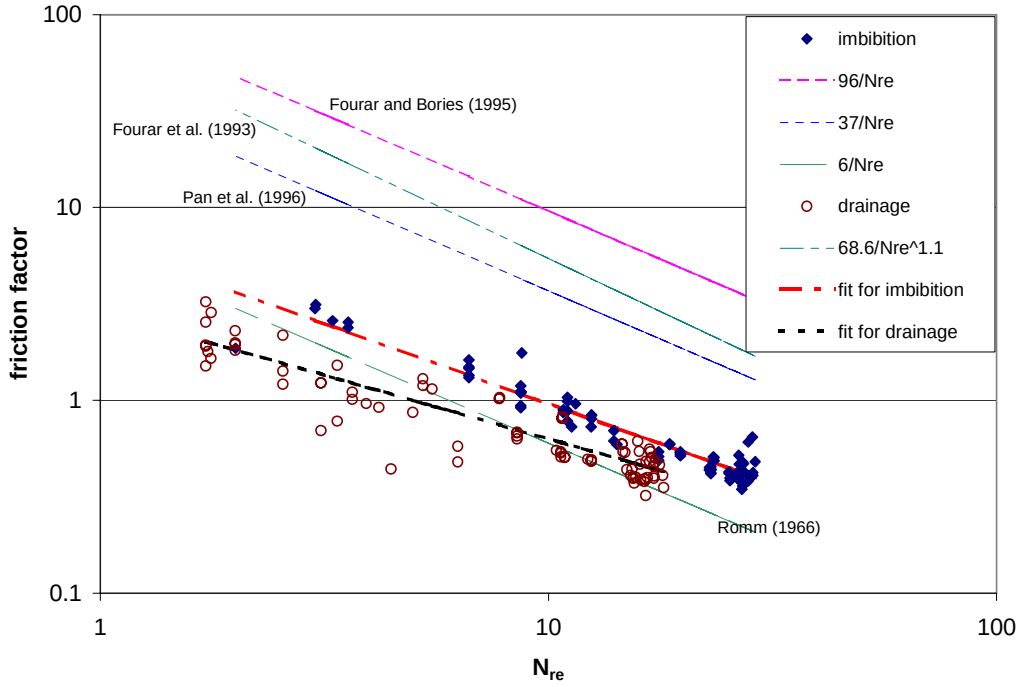

Figure 1.34 Friction factor with modified Reynold's number for rough-walled experiment.

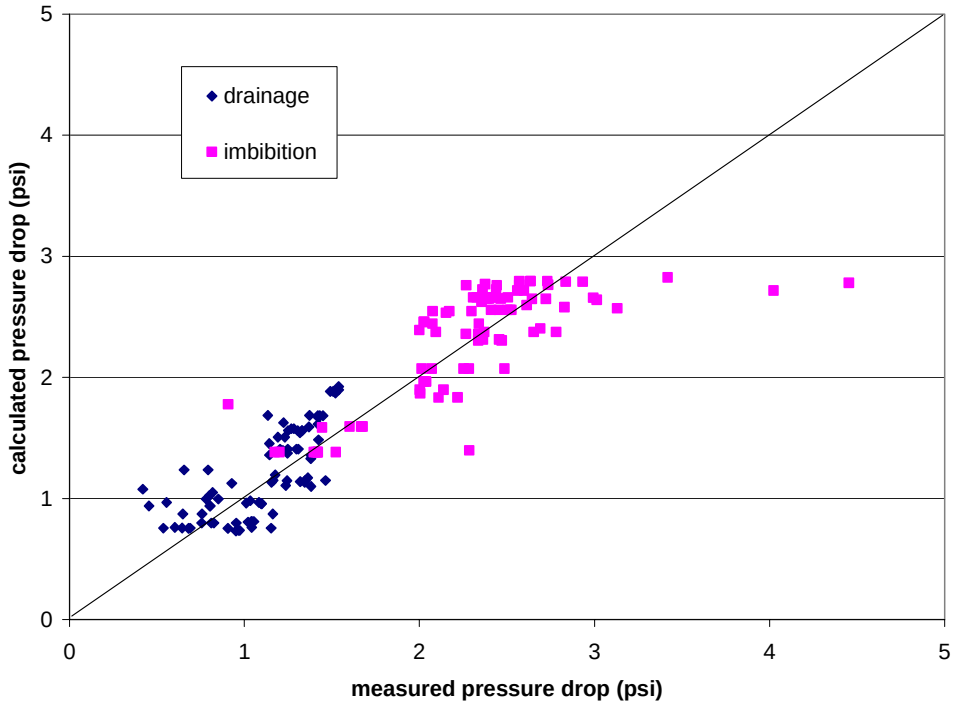

Figure 1.35 Comparison of the measured pressure drop against calculated pressure drop from homogeneous equivalent single-phase model.

Comparison of Smooth- and Rough-Walled Experiment to Other Studies

The data for both smooth and rough-walled experiments were entered in Figure 1.1 for comparison to previous studies and to known correlations for porous media (see Figure 1.36). Compared to other data, the experimental data in this study is higher than that of Persoff and Pruess (1995) experiments but lower than Persoff (1991). With this, no apparent conclusion can be made as to whether the data from this study contradict or agree with previous relative permeability experiments. However, more importantly Figure 1.36 shows that the experimental data mostly conform to Corey type of relative permeability curve. This suggests that flow through fractures can be analyzed by treating it as limiting case of porous media and by using the relative permeability variable. The relative permeabilities as seen in Figure 1.36 for fractures sum up to less than one and are not in linear relationship with saturation as suggested by the X-curve. This reiterates results from previous studies that phase interference in fractures does occur. Comparing the results for smooth and rough fractures, the relative permeability values for the smooth and the rough-walled drainage experiment do not differ much. However, the relative permeability for imbibition experiment in the rough-walled fracture is lower than these two experiments.

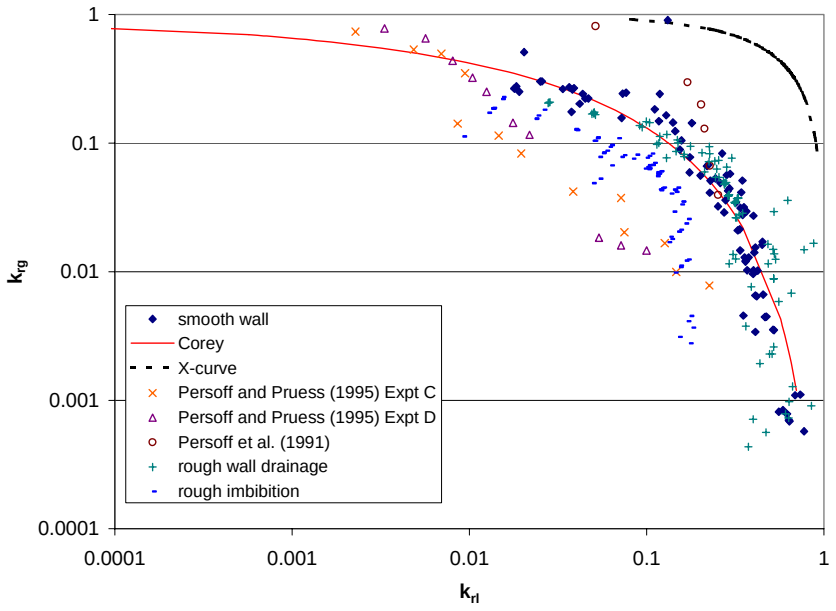

Figure 1.36 Comparison of relative permeability data with previous work on rough-walled fractures.

1.4 CONCLUSIONS AND RECOMMENDATIONS

The experiments and analysis presented in this paper have led to the following conclusions:

Two-phase flow through smooth and rough parallel plate fractures is characterized by each phase establishing localized continuous flow paths. The stability of these flow paths

is dependent on the flow rate ratio of the phases. A phase flow path undergoes constant cycles of breakage and reformation as certain points are blocked and unblocked by the other phase. The breaking and reforming of phase paths cause pressure, flow rate and saturation fluctuations even at constant input conditions. This reveals the unsteady nature of flow through fractures.

The imbibition process through a rough-walled fracture also undergoes wave-like flow similar to flow in pipes at high gas-water ratio. Other than this, flow through smooth- and rough-walled fractures is more similar to flow in porous media where a phase moves by establishing continuous channels. The flow mechanism of having moving discontinuous flow structures as bubbles or "islands" carried along by another continuous phase was not observed throughout the experiments.

Two-phase flow through smooth- and rough-walled fractures can be modeled adequately by a porous medium approach. In this approach, Darcy's law governs flow and phase interference is represented by the relative permeability variable. The resulting relative permeability curve from experimental data shows a clear relationship between relative permeability and phase saturation. The experimental relative permeability curves follow the Corey shape and can be fitted to reasonable accuracy by the Honarpour expression.

There is considerable phase interference in flow through fractures. This is deduced from the sum of the gas and liquid relative permeability for all experiments being less than unity.

The equivalent homogeneous single-phase approach did not give satisfactory representation of flow through fractures. The graphs of experimentally derived friction factor with the modified Reynold's number do not reveal distinctive linear relationship. This leads to inadequate pressure drop prediction of the model.

The apparatus and methodology used in this study proved to be an effective means of investigating flow through fractures. However, improvement is needed to ensure control of fracture aperture i.e. preventing the glass plate from being lifted by the flowing fluids. The method for saturation measurement is dependable when picture quality is good and when distinct boundaries of phases are seen. It is recommended to experiment with techniques for enhancing picture color contrasts. This will improve the program's accuracy in differentiating phases. This will be useful for cases when small isolated phases are dispersed throughout, such as the case in imbibition for rough-walled fractures.

It is recommended that further experiments with smooth-walled fractures be done this time with certainty as to the fracture absolute permeability. This is to establish the magnitude of relative permeability in smooth-walled fractures. It is also recommended to conduct experiments to investigate other variables in fracture flow that were not included in this study, such as effect of aperture, viscosity, gravity, degree of roughness, etc.

1.5 NOMENCLATURE

A = area

b = fracture aperture

C = constant in Blasium equation

f = friction factor

k_{abs} = absolute permeability

k_r = relative permeability

L = fracture length

n = constant in Blasium equation

N_{Re} = modified Reynold's number

p = pressure

Q = volumetric flow rate

q_l = Darcy flow velocity

S = saturation

V = superficial velocity

w = fracture width

Π = fracture perimeter

μ = viscosity

ρ = density

Subscripts:

g = gas phase

i = inlet

l = liquid phase

m = mean

o = outlet

r = residual

w = water

2. STEAM-WATER CAPILLARY PRESSURE

This research project is being conducted by Research Associate Kewen Li and Professor Roland Horne. The objective of this project is to investigate the fundamentals of steam-water capillary pressures in steam-water flow. The purpose of this study is to infer the correct water saturation distribution and hence the correct capillary pressures curve from X-Ray CT measurements with beam-hardening effect taken into account.

2.1 SUMMARY

Water saturation distribution in the vertically positioned core was measured during water imbibition at different imbibition times using an X-Ray CT technique. After the water imbibition was completed, the capillary pressure curves were measured in both vertical and horizontal positions and the results were compared.

2.2 INTRODUCTION

In the last Quarterly Report (April-June 2001), we found significant differences in CT values between steam-water and air-water gravity drainage processes in the core. However, the steam-water and air-water capillary pressure curves could not be obtained because of the beam hardening in the vertical core while the CT scanner was positioned horizontally. In this quarter, we inferred the capillary pressure curve in the vertically positioned core with beam hardening and compared the results to those measured in the horizontally positioned core with little beam hardening effect.

2.3 THEORY

Capillary pressure is balanced exactly by the gravity force once the spontaneous water imbibition into the core sample has been completed. The equation is expressed as follows:

$$P_{ci} = \Delta\rho g h \tag{2.1}$$

where P_{ci} is the capillary pressure; $\Delta\rho$ is the density difference between water and steam or air; g is gravity constant and h the height. The water saturation in the core at h was measured by using the X-ray CT method. Water saturation is calculated as follows:

$$S_w = \frac{CT_{\exp}(T) - CT_{dry}(T)}{CT_{wet}(T) - CT_{dry}(T)} \tag{2.2}$$

where $CT_{wet}(T)$, $CT_{dry}(T)$ are CT numbers of the core when it is fully saturated by water and air respectively; $CT_{exp}(T)$ is the CT number of the rock when it is partially saturated by air, all at the same temperature T.

Porosity measured by the X-ray CT method is computed using the following expression:

$$\phi = \frac{CT_{wet}(T) - CT_{dry}(T)}{CT_{water}(T) - CT_{air}(T)} \tag{2.3}$$

here CT_{water} and CT_{air} are the CT numbers of water and air respectively.

Once the porosity is known, the water saturation can be calculated as follows:

$$S_w = \frac{CT_{\exp}(T) - CT_{dry}(T)}{\phi[CT_{water}(T) - CT_{air}(T)]} \tag{2.4}$$

2.4 EXPERIMENTS

Rock and Fluids. Distilled water was used as the liquid phase in this study; the specific gravity and viscosity were 1.0 and 1.0 cp at 20^{o}C. Air was used as the gas phase; the surface tension of water/air at 20^{o}C was 72.75 dynes/cm. The ceramic core sample was provided by Refractron Technologies Corp and was the same as used in the previous study (Quarterly Report of April-June 2001). The core had a porosity of 40.9%, a length of 25.0 cm, an inner diameter of 4.275 cm and an outer diameter of 6.287 cm. We did not measure the permeability of the core sample due to its special shape but the permeability was estimated to be over 15 darcy.

X-ray CT Scanner. Distribution of water saturation in the core sample was measured as a function of height using a Picker^{TM} Synerview X-ray CT scanner (Model 1200 SX) with 1200 fixed detectors. The voxel dimension was 0.5 mm by 0.5 mm by 5 mm, the tube current used was 50 mA, and the energy level of the radiation was 140 keV. The acquisition time of one image was about 3 seconds while the processing time was around 40 seconds.

Apparatus. A schematic of the apparatus to measure steam-water and air water capillary pressures is shown in Figure 2.1. The core system was assembled in an aluminum containment vessel.

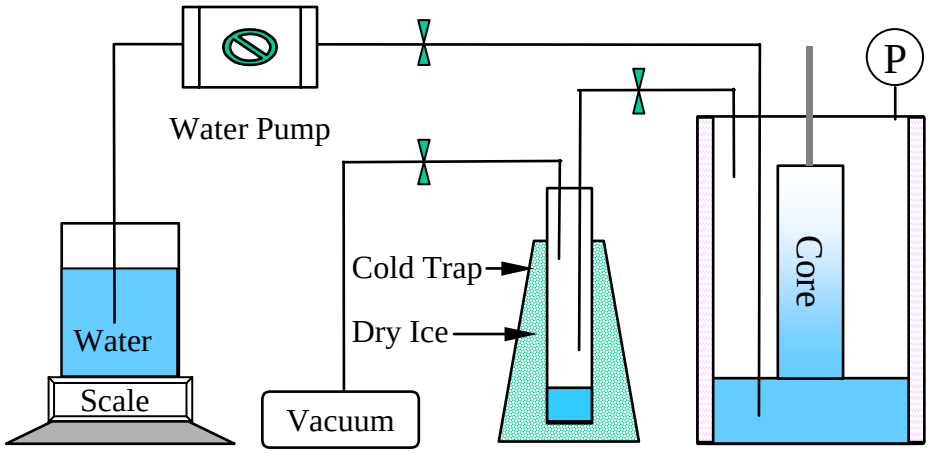

Figure 2.1: Schematic of the apparatus for steam-water and air-water capillary pressure.

A cold trap with dry ice was employed to protect the steam from entering the vacuum pump to extend its life and reduce the frequency of replacing the pump oil.

Water in the aluminum cylinder was delivered by the water pump (Dynamax, Model SD-200, manufactured by RAININ Instrument Co.) and the amount was measured by the scale (Mettler, Model PE 1600) with an accuracy of 0.01g and a range from 0 to 1600g.

Procedure. The core sample assembled in the aluminum cylinder was dried by heating while evacuating. An X-ray CT scan was made after the core was cooled to room temperature. The CT scanner was always positioned horizontally in this study. With the core positioned vertically in the horizontal scanner, the cross-section of the core in the scan plane is rectangular. This rectangular cross-section often results in beam-hardening artifacts in the CT image, since the tomographic algorithms are tuned for cross-sections that are roughly circular.

Water was injected into the aluminum cylinder. X-ray CT scans were made from time to time at specific amounts of water injected. The CT values should not change before the water touched the bottom of the core if there was no beam hardening effect. However it was clear that there was beam hardening effect in this case (because of the rectangular scan cross-section). The relationship between the CT values and the water column height in the aluminum cylinder were found at a specific position in the core. The relationship was then used to calibrate the effect of beam hardening. The water injection was stopped once water touched the bottom of the core (the water level was about one *cm* above the bottom of the core). The distribution of the CT value in the core was measured after the completion of the spontaneous water imbibition. The capillary pressure curve was inferred using the CT values calibrated using the relationship between the CT values and the water column height in the aluminum cylinder. The core sample was then removed from the aluminum cylinder immediately after the CT scan and was mounted horizontally in the scanner. Another X-ray CT scan was made and the capillary pressure could be calculated again using the CT values from this scan without beam hardening.

2.5 RESULTS

Water imbibition tests were conducted in air-water systems. Figure 2.2 shows the effect of the water column height (before water touched the bottom of the core) in the aluminum cylinder on the CT values of the left part of the core sample when the core was dry. The CT values were obtained by the ROI function of the software FP Image Viewer. We can see from Figure 2.2 that there are significant effects of the water column height in the aluminum cylinder on the CT values of the dry core sample in the lower part. The greatest effect is seen near the middle part of the core sample. There is very small effect at the top five *cm* in the core.

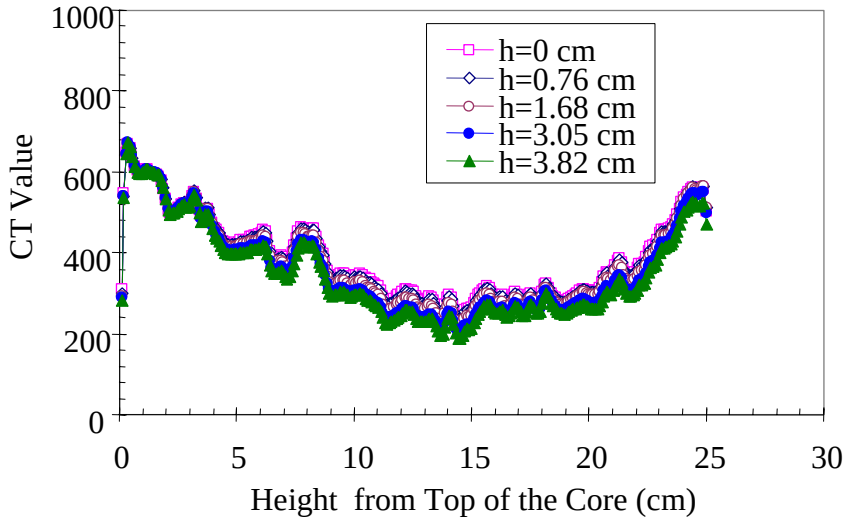

Figure 2.2: The effect of water column height in the aluminum cylinder on the CT values of the dry core sample.

A linear relationship between the CT value and the water column height in the aluminum cylinder was found at specific positions in the core sample. An example is shown in Figure 2.3. In this figure, "H" represents the distance from the top of the core sample and varies from 13.96 to 14.72 *cm*. We can see from Figure 2.3 that with more water in the aluminum cylinder, the CT values were lower in the core even though the fluid saturation in the core had not varied. The linear relationship shown in Figure 2.3 was used to calibrate the effect of the water column height on the CT values.

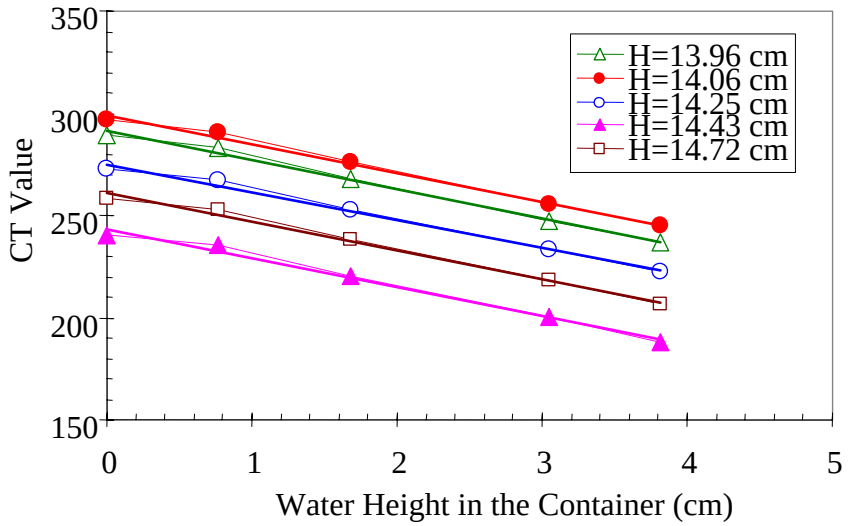

Figure 2.3: The relationship between the CT value and the water column height in the aluminum cylinder at specific positions in the core sample.

The distributions of CT values before and after water imbibition from the top to the bottom are shown in Figure 2.4. The movement of the water imbibition front can be seen clearly in this figure. The water imbibition was finished at about 3.5 hours after water contacted the core. We scanned the core about 24 hours later and found little change of CT values. Also seen is the effect of beam hardening. It should be observed that the more the water imbibed, the greater the CT value. It is true in the area near the bottom of the core. However the CT values in the area near the top of the core were smaller when more water was imbibed (see Figure 2.4).

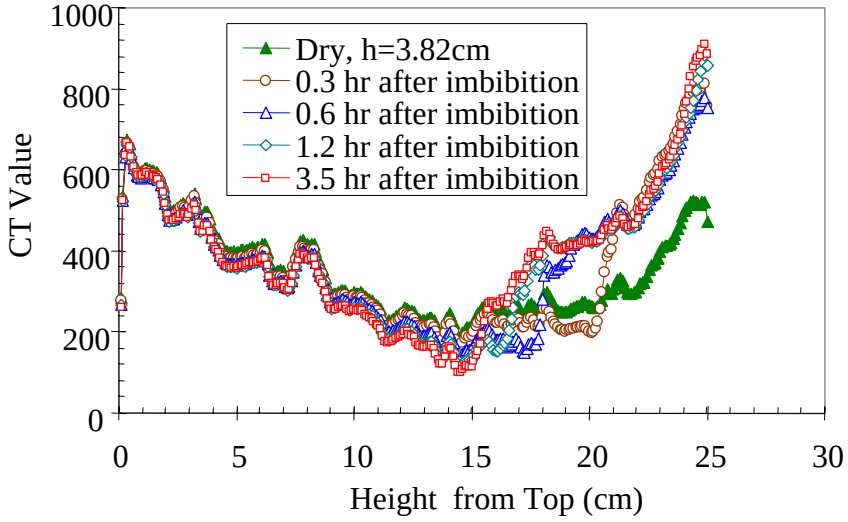

Figure 2.4: CT values before and after water imbibition in the core.

After the completion of water imbibition, the core was moved out from the aluminum cylinder and positioned horizontally in the coach. An X-ray CT scan was made through the core. Then the

core was dried and another X-ray CT scan was made. The CT values from the two scans are shown in Figure 2.5.

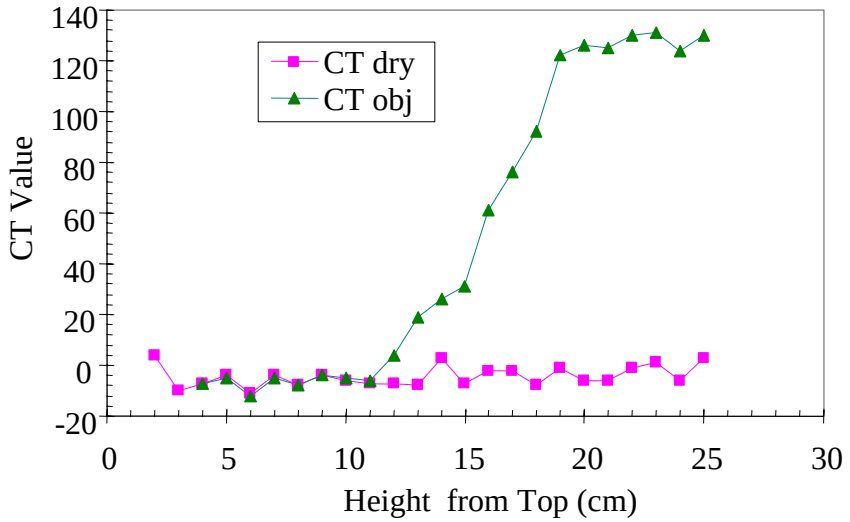

Figure 2.5: CT values of the core positioned horizontally.

Using the CT values shown in Figures 2.4 and 2.5, we could obtain two capillary pressure curves. The water saturation was calculated using Eq. 2.4. In the case of Figure 2.4, the CT values were calibrated using the linear relationships obtained from Figure 2.3. The distributions of the CT values before and after calibration of the beam hardening effect are shown in Figures 2.6 and 2.7 respectively.

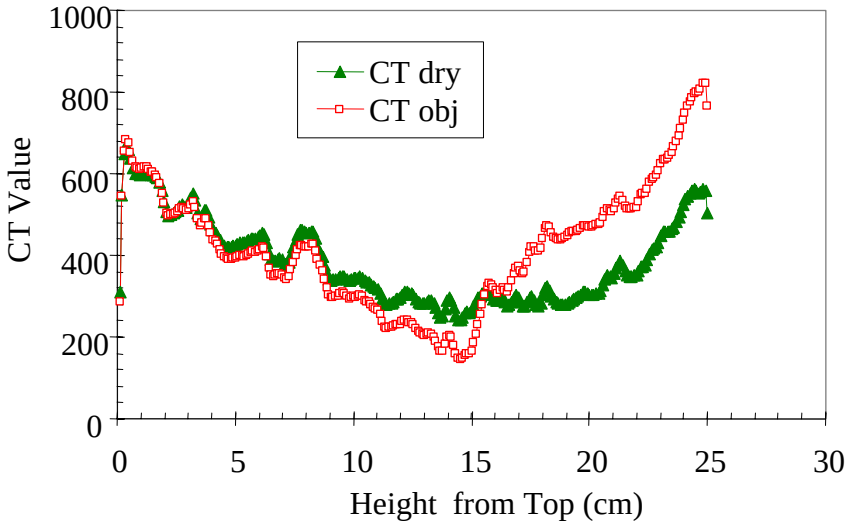

Figure 2.6: CT values of the core positioned vertically (before calibration).

As described previously, the CT values of the core after the completion of water imbibition should be greater or at least equal to that before the imbibition began when the core was dry. However we can see in Figure 2.6 that the CT values in the area near the

top of the core were smaller after the completion of water imbibition than those when the core was dry. This also shows the need to calibrate the effect of the beam hardening, as shown in Figure 2.7.

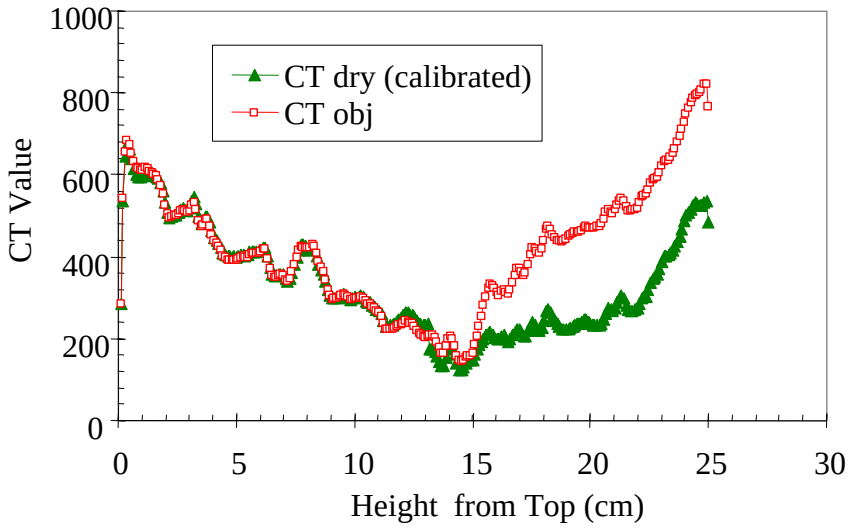

Figure 2.7: CT values of the core positioned vertically (after calibration).

The two capillary pressure curves should be closely equal. The results calculated for capillary pressures in two cases are shown in Figure 2.8.

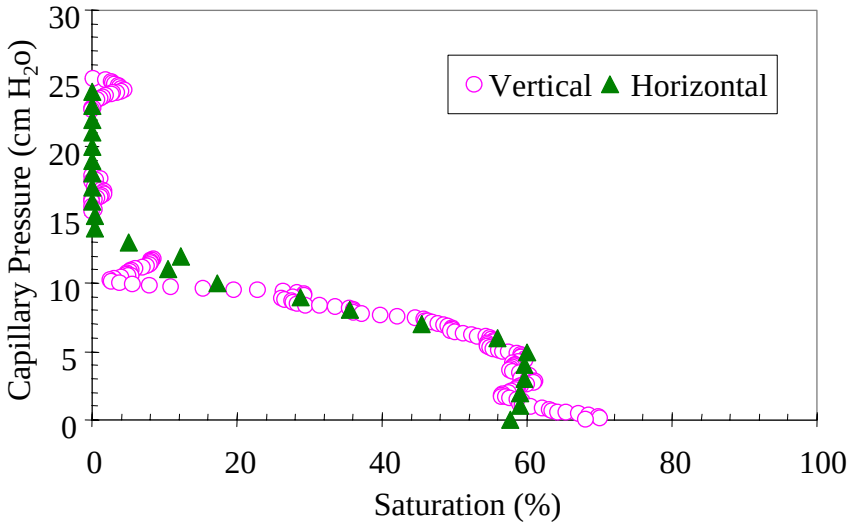

Figure 2.8: Capillary pressure curves obtained from different ways of positioning the core.

We can see from Figure 2.8 that the capillary pressure curve obtained from the CT values when the core was vertically positioned is roughly consistent with that when the core was

positioned horizontally. However, the capillary pressure data are more scattered when the core was positioned vertically.

2.6 CONCLUSIONS

Based on the current results, the following conclusions may be drawn:

1. The effect of beam hardening on the CT value is significant when the core is placed vertically in the scanner. A linear relationship between the CT value and the water column height in the container was found to compensate for this effect.
2. After the calibration to compensate for the beam hardening effect, the capillary pressure curve calculated from the CT values when the core was positioned vertically is roughly equal to that when the core was positioned horizontally.
3. The process of spontaneous water imbibition could be monitored using the X-ray CT technique even with the core was positioned vertically while the scanner was in horizontal mode. However, the data were noisier.

3. FRACTURED ROCK RELATIVE PERMEABILITY

This project is being conducted by Research Assistant Mark D. Habana, Research Associate Kewen Li and Prof. Roland N. Horne. The objective is to measure relative permeability relations for steam and water flow in a fractured geothermal rock. This work is an extension of current studies of steam-water flows, which have so far considered only artificially uniform porous rock. This quarter, the Jones and Roszelle method was used to calculate relative permeability values for the nitrogen-water relative permeability experiment.

3.1 BACKGROUND

Various works on flow through fractures have shown different kinds of relative permeability behavior. Experimental studies by Persoff and Pruess (1995) resulted in curves that can not be classified either as Corey type or as linear (X-curve) type. Fourar et al. (1993) suggested that multiphase interaction in a fracture is a function of flow velocity and therefore relative permeability is not the appropriate way to describe multiphase flow in fractures.

Past experiments have used synthetic fabricated fractures and/or gas-water or oil-water as fluids. This experimental study will use a real fractured core from The Geysers geothermal field to study steam-water relative permeability.

Nitrogen and helium permeability experiments were conducted on the core to determine the effects of the rock fractures and to investigate the constraints and practicalities of conducting multiphase flow experiments in real geothermal rocks. The core contains several fractures as determined from an X-ray computer tomography image.

3.2 EXPERIMENTAL METHODOLOGY

The rock permeability was measured using nitrogen and helium gas at room temperature. Since gas permeability is a function of pressure, as described by Equation 3.1, the flow measurements were conducted at a series of different mean pressures.

$$k_{gas} = k_{abs}\left(1 - \frac{b}{p_{ave}}\right) \qquad (3.1)$$

The core sample was obtained from a depth of 1409.3m at The Geysers geothermal field. The core is 6.91 cm in length and 4.70 cm in diameter.

At different confining pressures nitrogen was flowed into the core. Confining pressure from 500 to 850 psig was applied by injecting nitrogen around the heat shrink tubing inside the core holder. To apply a confining pressure of 1150 psig water was used in place of nitrogen.

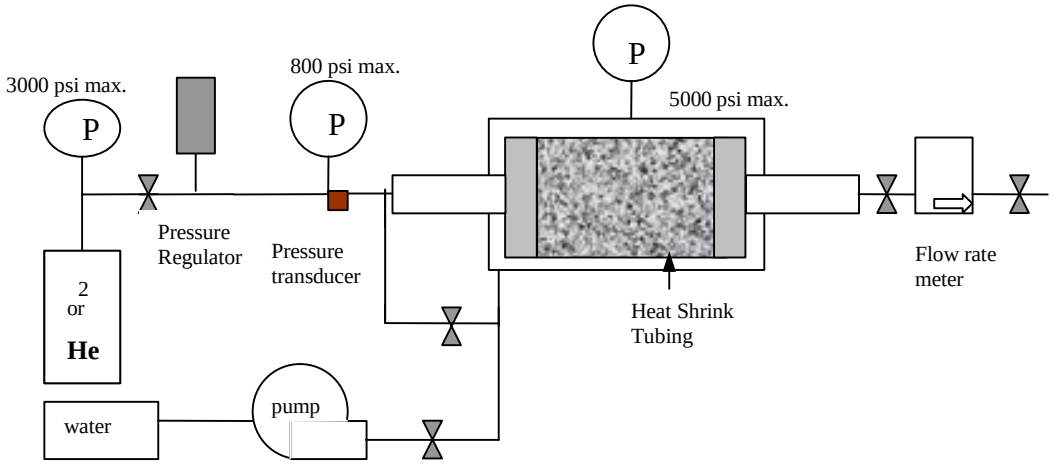

Figure 3.1: Apparatus for flow measurement in geothermal rock.

A pressure gauge and a pressure transducer connected to a digital display measured pressure at the inlet. The pressure at the outlet was taken to be 1 atm. The flow rate at the outlet was measured using a Matheson flow rate meter and controller (Model 8272-MF2000). The flow rate transducer calibration equation used was that determined by Kewen Li when he used the device in his experiments on slip factors (Quarterly Report Oct-Dec 1999).

For the nitrogen-water relative permeability experiment, at a confining pressure of 850 psig, water was pumped into the core up to irreducible gas saturation. Irreducible gas saturation was determined at the cessation of gas flow viewed in the translucent outlet tube (Figure 3.2). Then, nitrogen gas was pumped to displace the water in the core.

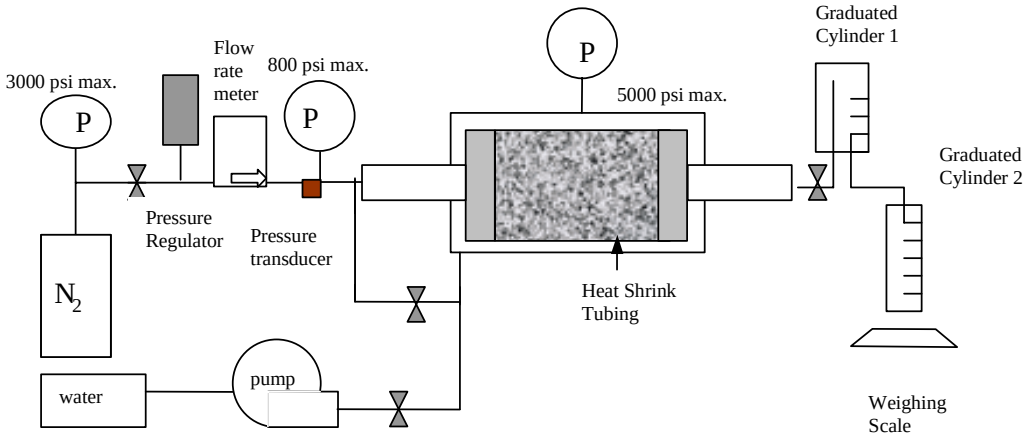

Figure 3.2: Nitrogen-water relative permeability experiment apparatus.

The flowmeter was placed upstream of the inlet. The first graduated cylinder was filled with water and inverted while the second graduated cylinder was placed on a weighing scale. The gas coming out of the core was trapped in the first cylinder and the displaced water flowed into the second cylinder. The water in the second cylinder is equal to the sum of the volume of the gas in the first cylinder and the water from the core outlet.

3.3 PARTIAL RESULTS AND DISCUSSION

Results of the nitrogen experiments are shown in Figure 3.3.

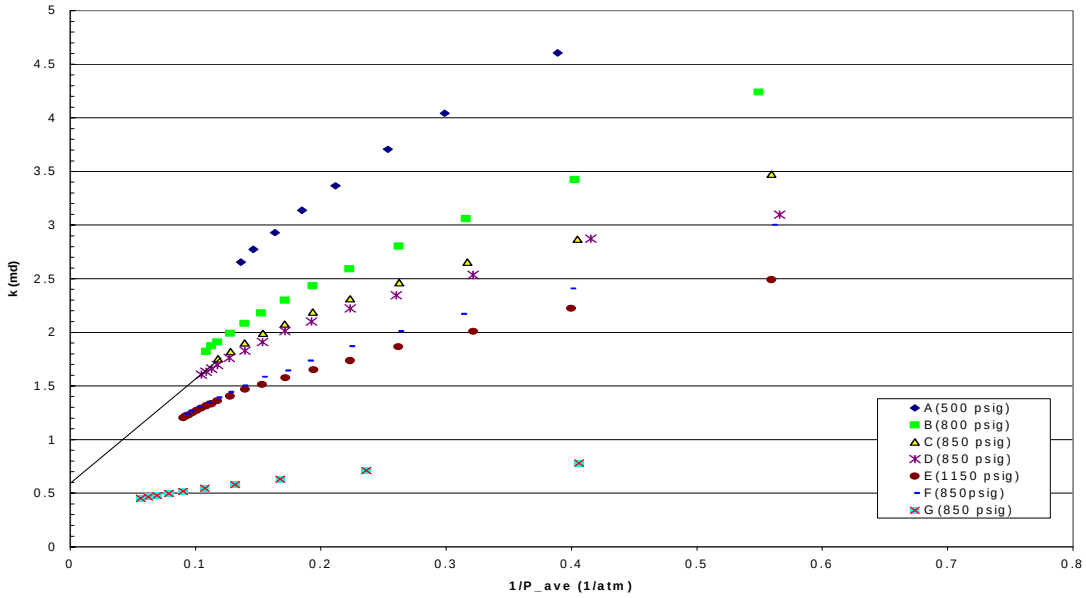

Figure 3.3: Nitrogen permeability as a function of pressure.

The intersection of the extrapolated lines with the vertical axis in the plot of permeability (k) versus the reciprocal of the mean pressure ($1/p_{ave}$) is taken to be the absolute permeability of the rock. At a confining pressure of 850 psig the absolute permeability is approximately 0.56 md. The permeability values labeled G was done recently and differs from other permeability curves at 850 psig. This is due to the core being wet after the nitrogen-water relative permeability experiment.

The equation for obtaining the inverse average effective viscosity, $\overline{\lambda^{-1}}$, in the Jones and Roszelle method was modified to take into account the Klinkenberg effect. Jones and Roszelle expressed the inverse average effective viscosity as Equation 3.2:

$$\overline{\lambda^{-1}} = \mu_b \left(\frac{\Delta p}{q}\right) / \left(\frac{\Delta p_b}{q_b}\right) \qquad (3.2)$$

where μ_b is the viscosity of the fluid used to find absolute permeability. For a gas, $\mu_b\ (\Delta p_b/q_b\ )$ is not a constant and should be replaced by $k_{abs}(A/L)$; where A is the cross-sectional area and L is the length of the core.

Application of the Jones and Roszelle procedure was not done successfully because of experimental data errors. A plot of calculated average nitrogen saturation versus pore volumes of nitrogen injected is shown in Figure 3.4. The gas saturations at the outlet derived from Figure 3.4 is shown in Fig. 3.5. Negative gas saturation values appear. This may be attributed to fluctuations of the weighing scale in the setup shown in Figure 3.2.

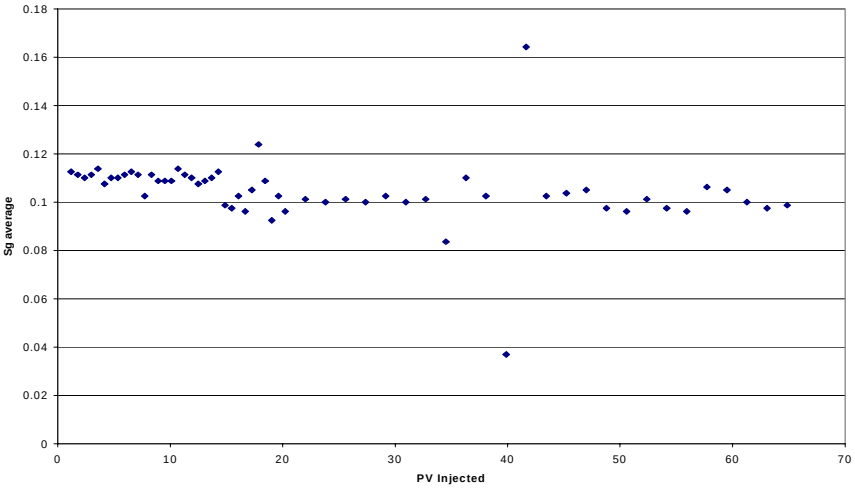

Figure 3.4: Average nitrogen saturation versus pore volumes of nitrogen injected.

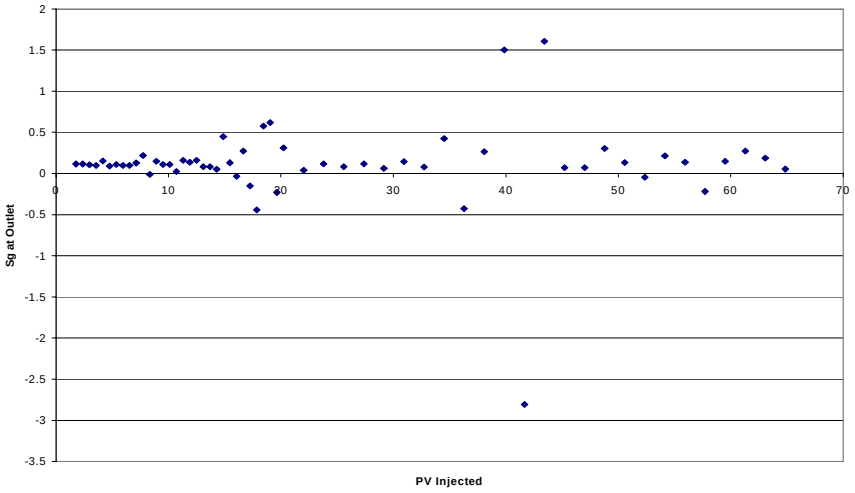

Figure 3.5: Outlet nitrogen saturation versus pore volumes of nitrogen injected.

3.4 CONTINUING AND FUTURE WORK

The core is presently being dried prior to repeating the nitrogen-water relative permeability experiment.

The steam-water relative permeability experiment will follow. The steam-water relative permeability experiment will also be an unsteady state displacement process.

The Jones and Roszelle method will be further modified to take into account heat and mass transfer so that it will be applicable for the steam-water case.

4. USING ELECTRICAL RESISTIVITY TOMOGRAPHY TO DETERMINE WATER SATURATION

This research project is being conducted by Research Assistants Chih-Ying Chen and Mark Habana, Research Associate Kewen Li, and Professor Roland Horne. The aim is to use electrical resistivity tomography (ERT) technology to determine the water saturation distribution in cores and then use this data in steam-water relative permeability and capillary pressure measurement. The main reason to do this is to gain advantage over X-ray CT methods which are not very practical for long-duration experiments in low permeability rocks such as most geothermal reservoir materials. An ERT test for two sandstone cores was finished and showed a highly sensitive response of the resistance at different water saturations. A combined X-ray/ERT experiment has determined the relationship between water saturation and resistance in different layers.

4.1 BACKGROUND

Using the resistivity to determining the saturation has been widely used in both geological and environmental fields. The relationship of the electrical resistivity and water saturation can be represented by the following equation:

$$I = bS_w^{-n} \tag{4.1}$$

where $I=R_t/R_o$, the resistivity index; R_t is the saturation measured; R_o is the resistivity of the rock when fully saturated with water; b is some function of tortuosity; and n is the saturation exponent. Empirically, n is equal to 2 according to Archie's relation (Archie, 1942). As we know, the capillary pressure and relative permeability are also functions of the saturation. If the relationship of the resistivity and capillary pressure can be established, an easier resistance measurement can be utilized to infer the corresponding capillary pressure, which is often more difficult to measure. In the steam-water relative permeability experiments, the ERT method will be used to measure saturation in the geothermal core. This saturation measurement technique is more appropriate than X-ray CT method because of the long duration of the experiment and because of the application of high confining pressures in the planned steam-water relative permeability experiment (which would preclude the use of X-ray-transparent plastic coreholders).

In this study, the X-ray CT method was used to determine the water saturation distribution throughout the core. Then the measured resistance was correlated with the water saturation obtained from the CT scanner. The basis of the X-ray CT method is that different water content will produce different CT number response. The water saturation at a certain position is calculated by the following equation:

$$S_w = \frac{CT_{exp}(T) - CT_{dry}(T)}{CT_{wet}(T) - CT_{dry}(T)} \tag{4.2}$$

where $CT_{wet}(T)$, $CT_{dry}(T)$ are CT numbers of the core when it is fully saturated by water and air respectively; $CT_{exp}(T)$ is the CT number of the rock when it is partially saturated by water, all of them are subjected to the same temperature T.

4.2 PREVIOUS ERT TESTING RESULT

This test was finished and part of the result was presented in the quarterly report for Jan.-Mar. 2001. The samples tested are shown in Table 4.1. Installations of the electrodes are shown in Figure 4.1 and 4.2. Two different methods in installing electrodes were used. For the hollow sandstone core, two sets of electrodes were installed at different vertical heights on the cylindrical surface of the core, named the upper set and the lower set (see Figure 4.1). For the Berea sandstone core, two electrodes were installed in the two ends of the Berea sandstone core separately (see Figure 4.2). Both of these two tests were conducted during spontaneous drainage process. Cores were fully saturated with water by using vacuuming method, and then they were exposed in the atmosphere to start drying (drainage).

Table 4.1: Properties of samples tested

Sample	Size (mm)	Pore Volume (ml)	Porosity (%)	Position of electrodes
Hollow sandstone core	49.78 OD × 31.87 ID × 51.20 L	15.3	26	Around the core
Berea sandstone core	25.52 D × 50.12 L	6.46	25.20	Two ends

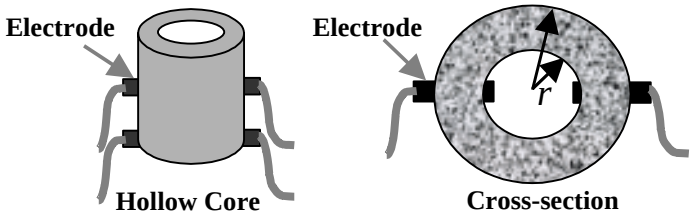

Figure 4.1: The installation of the electrodes in the hollow sandstone core.

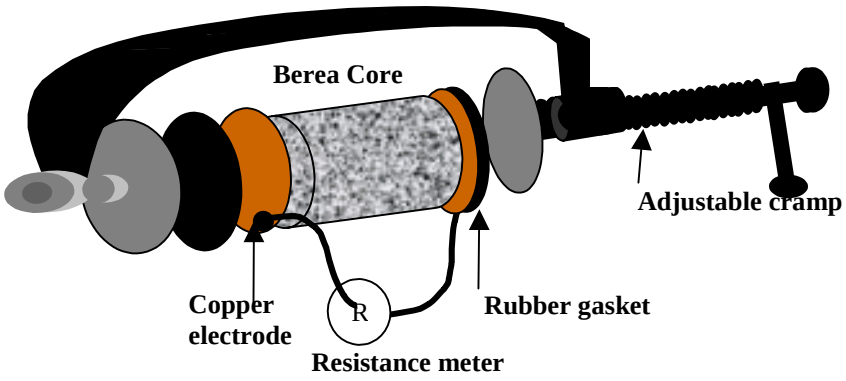

Figure 4.2: The installation of the electrodes in the Berea sandstone core.

Results are shown in Figure 4.3 and 4.4. Both tests showed a satisfactorily sensitive resistance response. The resistance curves are similar to a drainage capillary curve. Also in Figure 4.3, because only the average saturation was measured during this test, the upper resistance reading is different from the lower reading at some specific average saturation. To overcome this problem, a method using X-ray CT to measure the saturation at the cross section (layer saturation) where the electrode set was installed was designed.

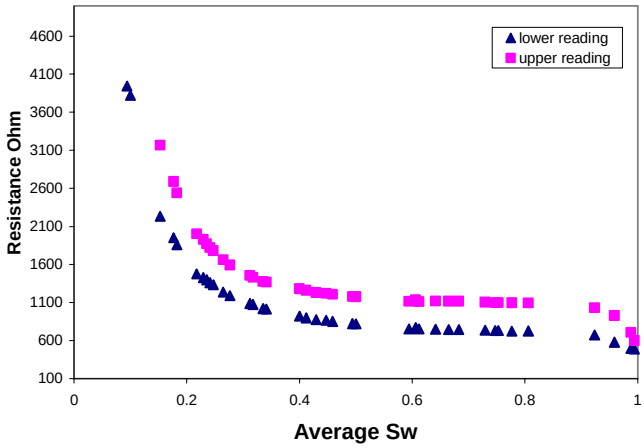

Figure 4.3: Measurements of resistances in the hollow sandstone core.

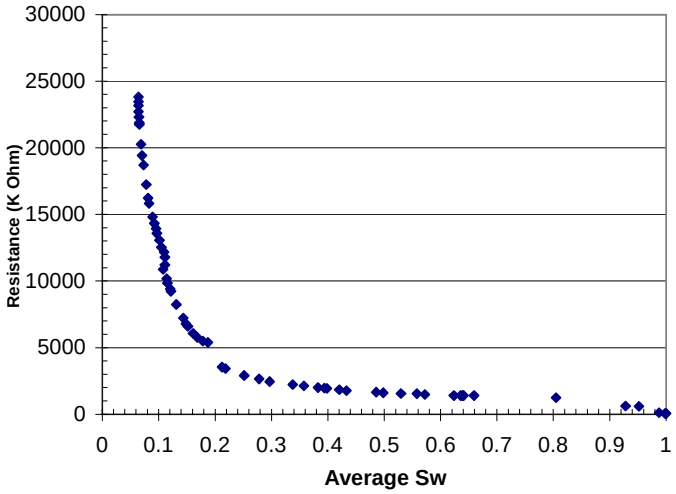

Figure 4.4: Measurements of resistances in Berea sandstone.

4.3 THE X-RAY ELECTRICAL RESISTIVITY TOMOGRAPHY EXPERIMENT

In this experiment, a 69mm diameter × 75mm length heterogeneous sandstone was used. Figure 4.5 shows the picture of the core sample. Table 4.2 shows the property of the core.

Figure 4.5: the heterogeneous shaly sandstone core.

Table 4.2: Properties of the sandstone core

Sample	Size (mm)	Pore Volume (ml)	Porosity (%)	Number of electrodes
Heterogeneous shaly sandstone	68.94 D X 75.53 L	35.2	12.5	24

The installation of electrodes is illustrated in the Figure 4.6. There were four layers of electrodes. Eight electrodes were installed in layers 2 and 3, numbered from 1 to 8. Electrodes in each of these two layers were separated by 45 degrees. Four electrodes were installed in layers 1 and 4, numbered 1, 3, 5 and 7 (in order to meet the same notation for the same position of the electrodes in layers 2 and 3). Electrodes in each of these two layers were separated by 90 degrees. The positions of each layer and electrode are shown in Figure 4.6. Electrodes, held in place by rubber sheets, are in direct contact with the core. 1-mm heat shrink tubing was wrapped around the core and the wires to decrease water evaporation.

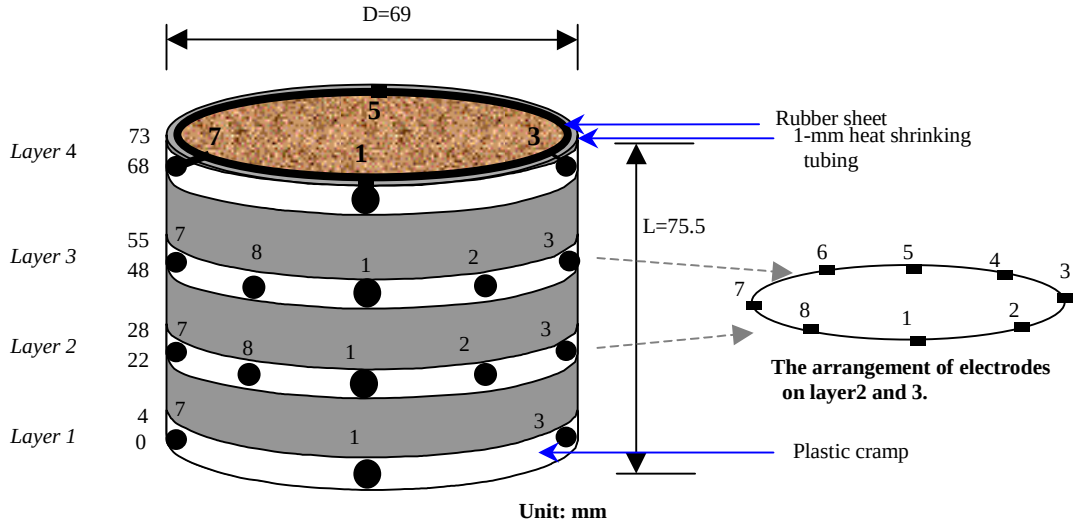

Figure 4.6: Schematic of the arrangement of electrodes of the heterogeneous shaly sandstone core.

The core was placed in the CT scanner so that the resistance readings and satruation measurement could be made at the same cross section of the core. Different amounts of deionized water were imbibed into the core and resistance readings were taken. A schematic and picture of the apparatus are shown in Figure 4.7 and 4.8.

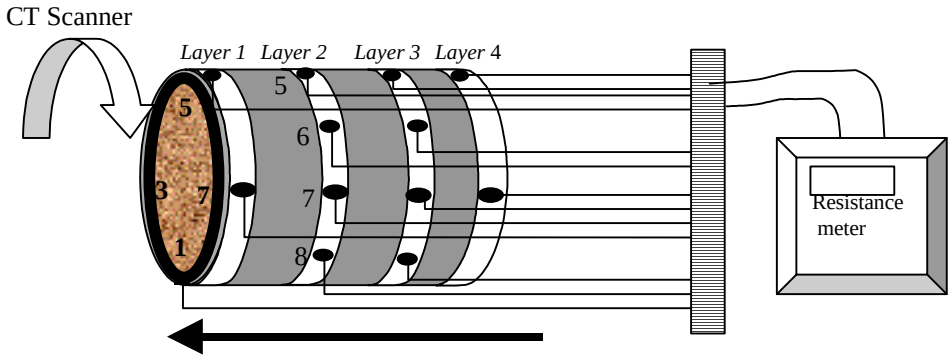

Figure 4.7: Schematic of the resistance measurement and CT scan of the core sample.

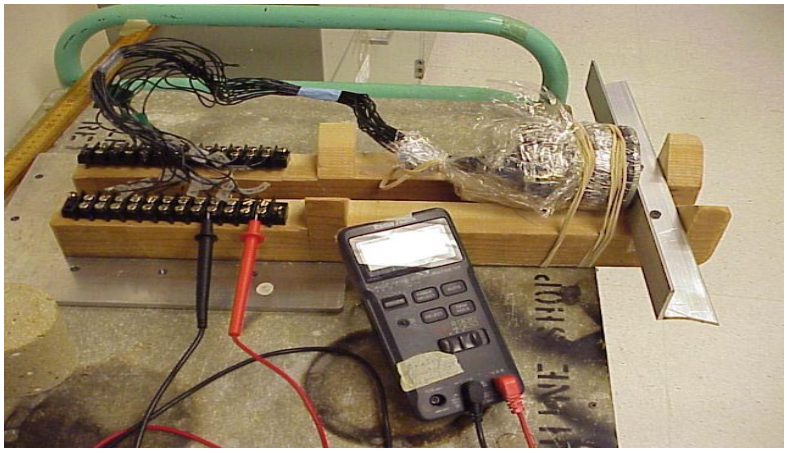

Figure 4.8: Picture of the resistance measurement and CT scan of the core sample.

4.4 EXPERIMENT RESULT

A series of water imbibition procedures was conducted in the sandstone core. Every time after the core had imbibed a certain amount of water, the ERT core was wrapped in plastic film to prevent evaporation and placed on the CT positioning assembly for at least 12 hours to achieve a steady state water saturation distribution (see Figure 4.8). After that, the core was scanned in X-ray CT machine and the resistances from different electrode combinations were measured.

Figure 4.9 shows the distribution of the CT number at each 5mm of the core. The corresponding layer position is also shown in Figure 4.9. As can be seen, the CT number increases as the average water saturation increases. Higher CT numbers all gather near the top of the core sample except in the case when the saturation was 45%. This may be

because of the characteristic of the heterogeneity of the core, the time needed to reach static saturation condition.

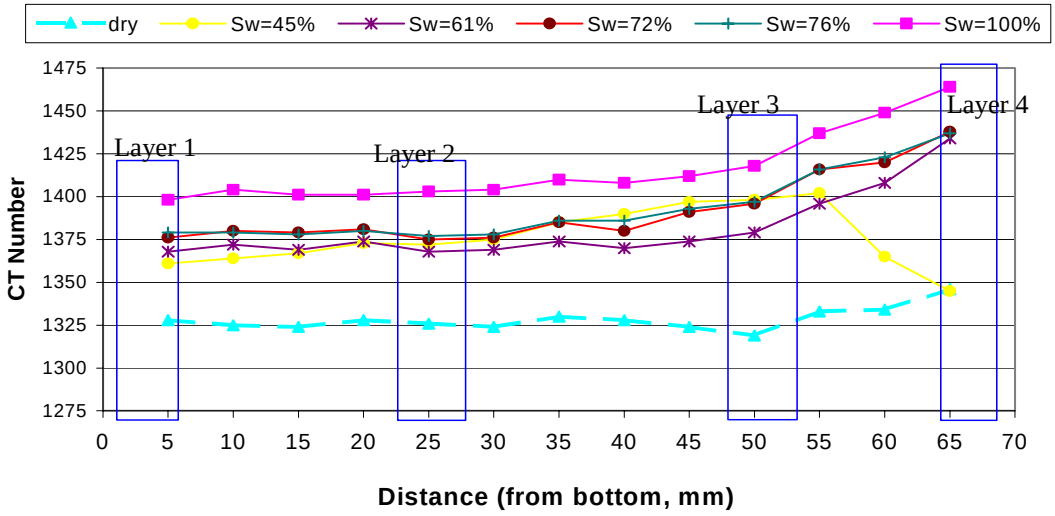

Figure 4.9: Distribution of CT number in the core sample along length.

For the resistance measurement, two different procedures were used. In order to construct the saturation distribution, both single-layer resistance and interlayer resistance were obtained. To simplify this preliminary experiment, the electrode numbered 1 in each layer was fixed in each resistance measurement for the single-layer model. The electrode numbered 1 in layer 1 was fixed in each resistance measurement for the interlayer model. The configuration of the measuring electrode set is illustrated in the Figure 4.10.

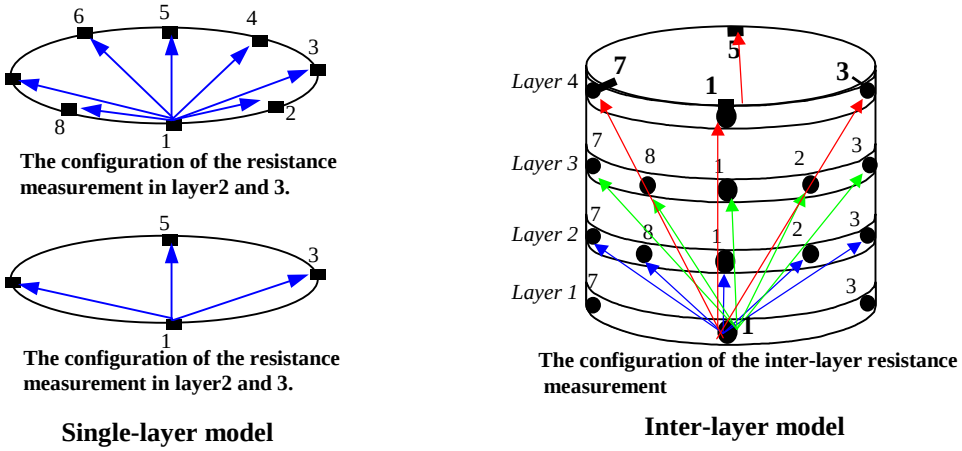

Figure 4.10: The configuration of the measuring electrode set of the single- and inter-layer model.

The resistance measurement result for the single-layer model is shown in Figures 4.11a to 4.11d. From Figures 4.11a and Figure 4.11b, the increase of the conductivity (reciprocal of the resistance) is consistent with the increase of average water saturation. However,

the conductivity of electrode 3 in layer 4 in 100% average water saturation is less than that of 76% water saturation (Figure 4.11b). Furthermore, more abnormal readings are found in Figures 4.11c and 4.11d. Some of the resistance readings are inconsistent with the saturation change, especially in the fully saturated condition.

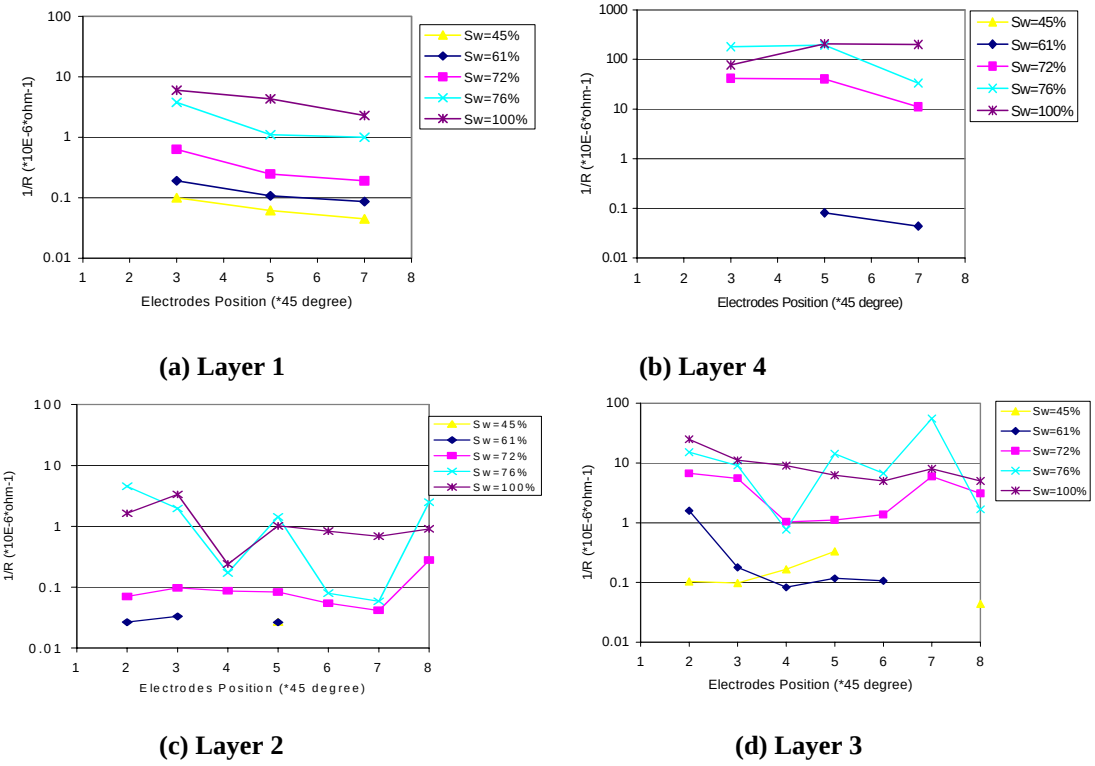

(a) Layer 1 **(b) Layer 4**

(c) Layer 2 **(d) Layer 3**

Figure 4.11: The reciprocal of the resistance (conductivity) vs. average water saturation in the single-layer model.

Figures 4.12a to 4.12c show the resistance measurement result for the interlayer model. Again, the increase of the conductivity (reciprocal of the resistance) is consistent with the increase of average water saturation except when the core was fully saturated.

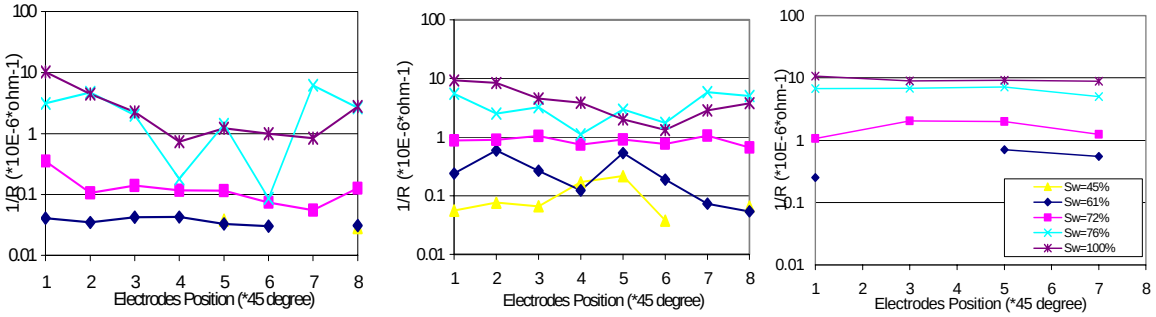

(a)Layer1-2 **(b) Layer1-3** **(c) Layer1-4**

Figure 4.12: The reciprocal of the resistance (conductivity) vs. average water saturation in the inter-layer model.

According to the CT number distribution in Figure 4.9, the water saturation distribution was nonuniform in the core. In most of the cases, the saturation increases as a function of length. The water saturation in each layer of the core was calculated according to Equation 4.2 and the related position of layers in Figure 4.9. Figure 4.13 shows the resistance inferred water saturation in different layers instead of average water saturation.

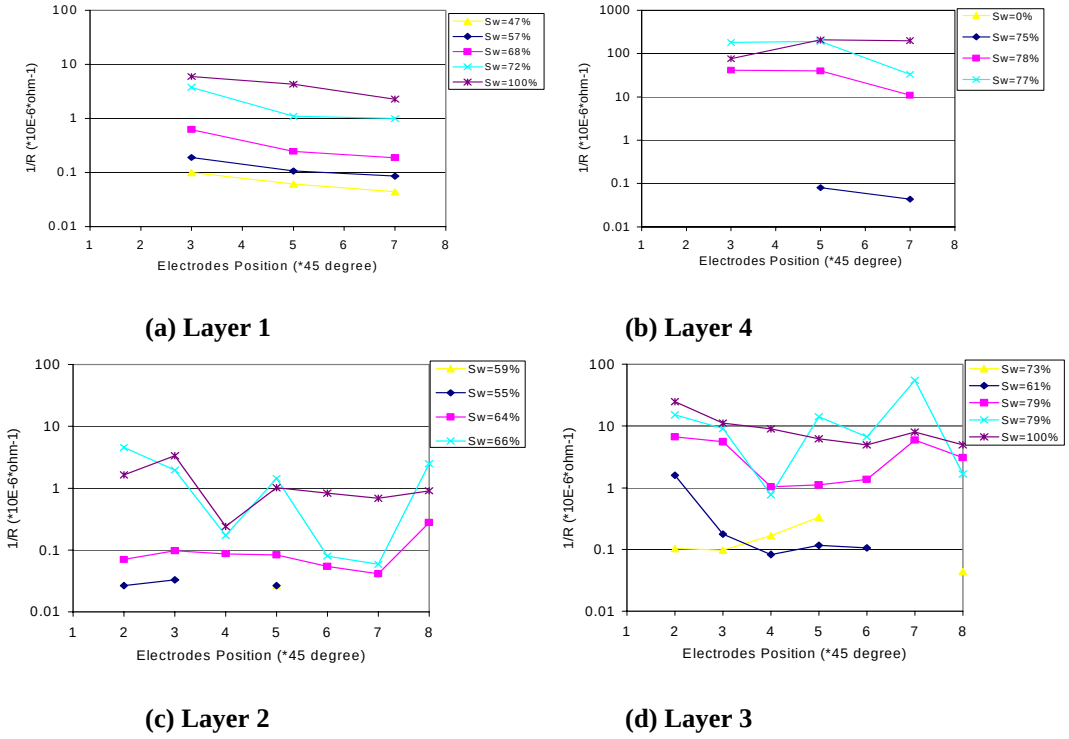

(a) Layer 1 **(b) Layer 4**

(c) Layer 2 **(d) Layer 3**

Figure 4.13: The reciprocal of the resistance (conductivity) vs. layer water saturation in the single-layer model.

Comparing Figure 4.11 and Figure 4.13, the resistances measured from electrodes in layers 1 and 4 are consistent with saturation change except for the measurement at electrode 3 in layer 4 at Sw=100%. In layer 2 and layer3 (Figure 4.11c, 4.11d and Figure 4.13c, 4.13d) we can see the trend of the conductivity is roughly consistent with the trend of the water saturation. However, there are some electrodes that have abnormal readings in each layer. This may be due to several reasons. The attachment of the electrodes to the cylindrical surface of the core may be the main reason. Even though rubber sheets, plastic clamps and heat-shrink tubing were used to hold the electrodes firmly in contact with the surface of the core, some bad electrode contacts were still found when measuring the resistance (judged from the unstable resistance reading or overload reading). The measuring device plays another important role in the ERT. The portable multimeter used in this experiment was not very suitable for the high resistance, high sampling rate, high accuracy requirement measurement. The meter also could not acquire all the resistances simultaneously. The one-by-one resistance measurement was not only time-consuming but made it difficult to obtain an unbiased steady-state reading.

4.5 FUTURE WORK

The ERT test experiments showed some promise in determining the water saturation distribution in the sandstone core without having to use the X-ray CT scanner. However, the accuracy of the resistance measured is questionable. Some further redesign of the measurement hardware should be made. Future experiments will focus on increasing the number of electrodes, improving the contact of the electrodes and using multichannel data acquisition to record the resistance of all the electrodes simultaneously. For the software part, the saturation distribution reconstruction algorithm will be designed by using the numerical methods combining electric field simulation and parameter estimation algorithms.

5. SCALING OF SPONTANEOUS WATER IMBIBITION DATA

This research project was conducted by Research Associate Kewen Li and Professor Roland Horne. The goal of this study is to develop a method to scale the experimental data of spontaneous water imbibition (cocurrent) for gas-water systems. During this quarter, experimental data of spontaneous water imbibition at different values of initial water saturation in natural state Berea sandstone (without clay removed) were obtained.

5.1 SUMMARY

Previously (Quarterly Report April - June, 2001), we developed a method to scale the experimental data of spontaneous water imbibition for gas-liquid systems. In this method, we defined a dimensionless time with wettability and gravity included. The definition of the dimensionless time was not empirical but based on a theoretical derivation. In this study, it was verified experimentally that the spontaneous water imbibition data in chalk, The Geysers graywacke, and Berea sandstone with and without clay removed could be scaled using the new dimensionless time, including the data at different values of initial water saturation in Berea.

5.2 INTRODUCTION

Geothermal reservoirs are usually highly fractured. When water is injected in highly fractured reservoirs, the amount and the rate of water imbibition from the fracture into the matrix by spontaneous imbibition are essential to the understanding of reservoir performance. The process of spontaneous water imbibition is controlled by the properties of the porous medium, fluids, and their interactions. These include porosity, permeability, pore structure, matrix size and shape, boundary condition, fluid viscosity, initial water saturation, wettability, the interfacial tension, relative permeability, and gravity. Scaling spontaneous water imbibition is important to evaluate the production performance because so many factors are involved. In order to successfully scale the experimental data, it may be necessary to consider the effects of all the significant factors. Scaling has been investigated widely in oil-water systems but rarely in gas-liquid systems.

As pointed out by Zhang *et al*. (1996), when the routine dimensionless time suitable for oil-water systems was used to scale the experimental data in gas-liquid systems, the results were scattered significantly. Therefore, we developed a method to scale the experimental data of spontaneous water imbibition (cocurrent) for gas-water systems using a newly defined scaling group with almost all the factors included. This method was verified experimentally by data from different rocks with different size, porosity, permeability, initial water saturation, and wettability. During this quarter, experimental data of spontaneous water imbibition at different values of initial water saturation in natural state Berea sandstone were analyzed.

5.3 THEORY

In the last report (Quarterly Report April - June, 2001), we derived the following equation based on the work of Li and Horne(2001):

$$(1-R^*)e^{R^*} = e^{-t_d} \tag{5.1}$$

where

$$t_d = c^2 \frac{k_w}{\phi} \frac{P_c}{\mu_w} \frac{S_{wf} - S_{wi}}{L_a^2} t \tag{5.2}$$

where t_d is the dimensionless time with gravity and capillary forces included, L_a is the characteristic length, μ_w is the viscosity of water, S_{wi} is the initial water saturation, and S_{wf} is the water saturation behind the imbibition front; k_w and P_c are the effective permeability of water phase and the capillary pressure at a water saturation of S_{wf}. c is a constant representing the ratio of gravity and the capillary forces, which is expressed as follows:

$$c = \frac{b}{a} \tag{5.3}$$

and

$$a = \frac{Ak_w(S_{wf} - S_{wi})}{\mu_w L} P_c \tag{5.4}$$

$$b = \frac{Ak_w}{\mu_w} \Delta\rho g \tag{5.5}$$

R^* is the normalized recovery, which is expressed as follows:

$$R^* = cR \tag{5.6}$$

here R is the recovery by water imbibition in terms of pore volume.

We can see from Eq. 5.1 that R^* is only a function of the newly-defined dimensionless time with gravity and capillary forces included. This feature shows that experimental data from spontaneous water imbibition in rocks with different size, porosity, permeability, initial water saturation, interfacial tension, and wettability can be scaled to a single curve of R^* vs. t_d.

As a comparison to the dimensionless time defined in Eq. 5.2, the existing dimensionless time without gravity and capillary forces included is usually defined as follows (Ma *et al.*, 1995):

$$t_D = \sqrt{\frac{k}{\phi}} \frac{\sigma}{\mu_m L_a^2} t \tag{5.7}$$

where t_D is the dimensionless time, k is the rock permeability, ϕ is the porosity, σ is the interfacial tension between oil and water, t is the imbibition time, μ_m is the geometric mean of water and oil viscosities and L_a is the characteristic length.

5.4 EXPERIMENTS

Chow *et al*. (1999) conducted tests of spontaneous water imbibition (cocurrent) both in Berea sandstone without clay removed, as well as in chalk. The experimental data from this study were used to verify the scaling method represented in Eq. 5.1.

Fluids. Air was used as the gas phase and distilled water as the liquid phase. The surface tension of water/air at 20°C is 72.75 dynes/cm.

Core Samples. The Berea sandstone sample had a permeability of around 500 md and a porosity of about 21.2%; its length and diameter were 9.962 cm and 4.982 cm. The permeability of the chalk sample was around 5 md; its length and diameter were 7.5 cm and 2.54 cm, respectively.

5.5 RESULTS

The relationships between the quantity of water imbibed into the Berea sandstone and the time at five different initial water saturations are shown in Figure 5.1. The amount of water imbibed decreases with an increase of initial water saturation.

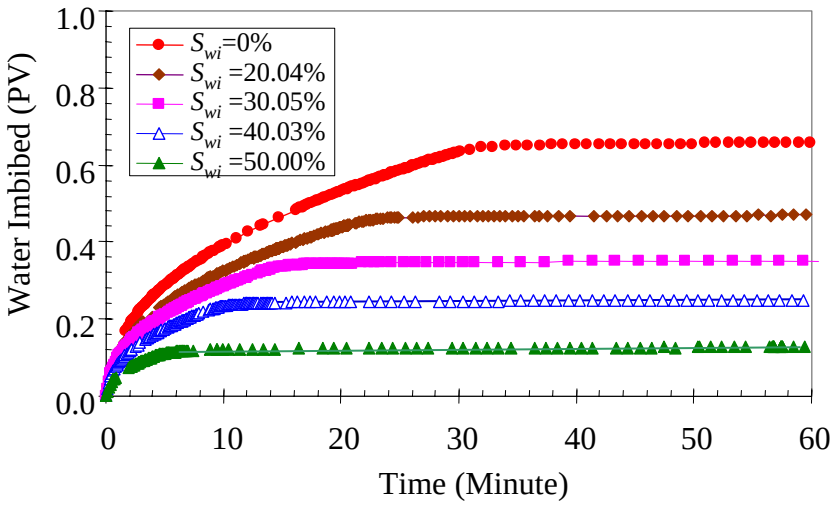

Figure 5.1: Spontaneous water imbibition behavior in Berea sandstone.

Figure 5.2 shows the scaling results for the spontaneous water imbibition data at five different initial water saturations using the existing dimensionless time defined in Eq.5.7. Note that only water viscosity was used in the scaling. The geometric mean viscosity term in Eq. 5.7 was substituted by the viscosity of water. It is supposed that all the experimental data points obtained at different initial water saturations should sit close to a single curve if the dimensionless time is appropriate for the scaling. However, Figure 5.2 demonstrates that the experimental data points scatter significantly.

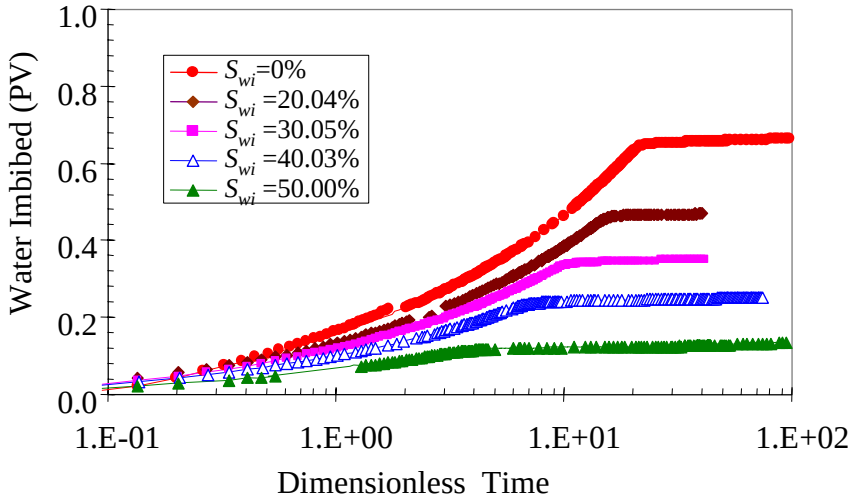

Figure 5.2: Scaling using existing dimensionless time for Berea sandstone at different initial water saturations.

Fig. 5.3 shows scaling results in terms of recoverable recovery using the existing scaling model for the same experimental data used in Fig. 5.2. The data points are also scattered very much.

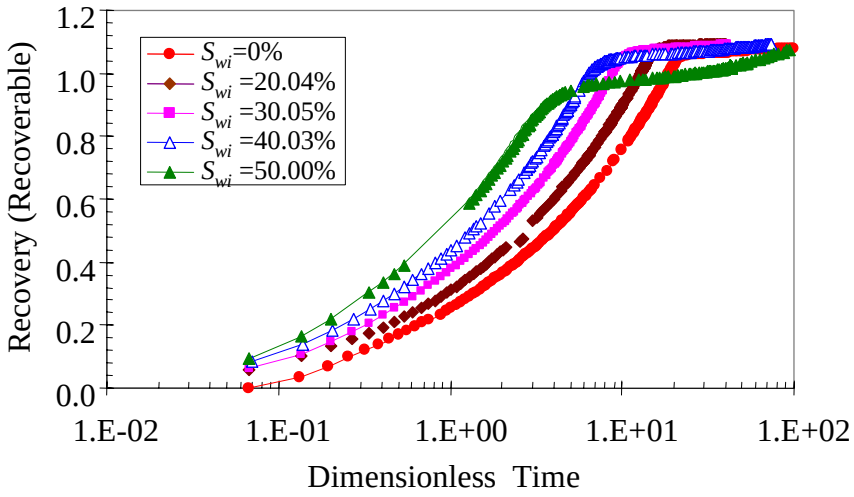

Figure 5.3: Scaling using existing dimensionless time for Berea sandstone at different initial water saturations in terms of recoverable recovery.

Using the scaling group defined in Eq. 5.2, the same experimental data used in Figure 5.2 were scaled and the results are shown in Figure 5.4.

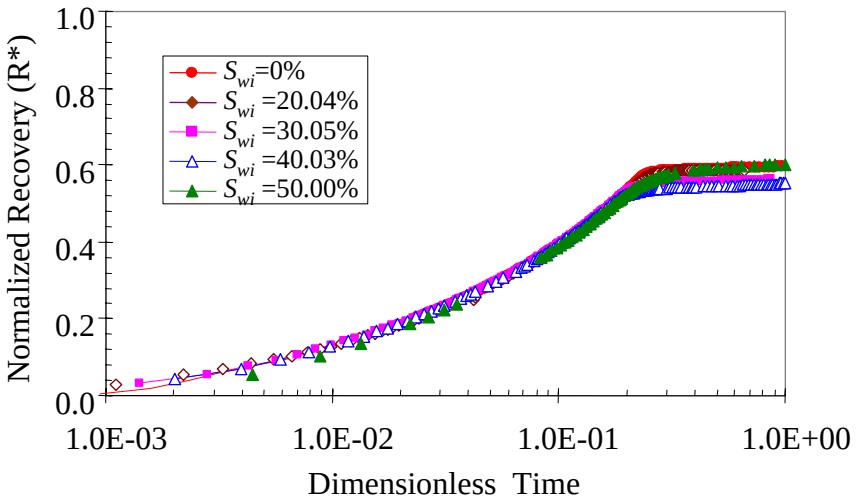

Figure 5.4: Scaling using the new scale model for Berea sandstone at different initial water saturations.

We can see from Figure 5.4 that the proposed scaling model works remarkably well for spontaneous water imbibition in Berea sandstone at different initial water saturations.

In order to verify the new scaling method in rocks with very different properties and at different initial water saturations, we plotted the experimental data of spontaneous water imbibition from Berea sandstone with clay removed by firing (Berea_1), Berea sandstone without clay removed (Berea_2), graywacke from The Geysers, and chalk in Fig. 5.5.

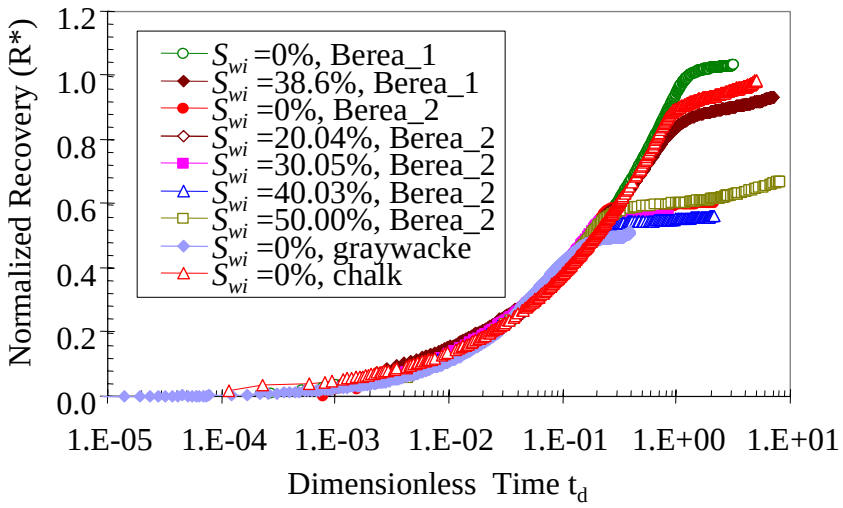

Figure 5.5: Scaling using the new scale model for rocks of very different property at different initial water saturations.

The permeability difference between the Berea sandstone and the graywacke was about in the order of 10^4. The porosity difference was about five times. We believed that the

wettability difference might also be large although there were few methods to identify this.

An excellent correlation between the normalized recovery and the new dimensionless time was obtained for all the experimental data of spontaneous water imbibition in different rocks and at different initial water saturations before the imbibition front contacted the top of the core sample.

5.6 CONCLUSIONS

Based on the present results, the following conclusions may be drawn:

1. The scaling model proposed by Li and Horne (2001) for gas-liquid systems was verified experimentally for rocks with very different properties and at different initial water saturations.
2. An excellent correlation between the normalized recovery and the new dimensionless time was obtained for all the present data of spontaneous water imbibition in different rocks before the imbibition front contacted the top of the core sample.
3. The existing scaling model could not scale the experimental data of spontaneous water imbibition in gas-liquid systems.

6. REFERENCES

Amyx, J. W., Bass, D.M, and Whiting, R.L.: *Petroleum Reservoir Engineering Physical Properties*, McGraw-Hill Book Co.,New York, 1960, pp 199-200.

Archie, G.E.: "The Electrical Resistivity Log as an Aid in Determining Some Reservoir Characteristic, "*Trans.* AIME, 1942.

Chow, K., Li, K., and Horne, R. N.: Section 4 in Quarterly Report for October-December 1999, Stanford Geothermal Program, DE-FG07-95ID13763.

Corey, A.T.: The Interrelationship Between Gas and Oil Relative Permeabilities, *Prod. Mon.*, Vol. 19, 1954, pp. 38-41.

Fourar, M. and Bories, S.: "Experimental Study of Air-Water Two-Phase Flow Through A Fracture (Narrow Channel)," *Int. J. Multiphase Flow* Vol. 21, No. 4, Toulouse, France (1995) pp. 621-637.

Fourar, M., Bories., Lenormand, R., and Persoff, P.: "Two-Phase Flow in Smooth and Rough Fractures: Measurement and Correlation by Porous-Medium and Pipe Flow Models," *Water Resources Research* Vol. 29 No. 11. November 1993, pp. 3699-3708.

Hanselman, D. and Littlefield, B.: *Mastering Matlab 5 A Comprehensive Tutorial and Reference*, Prentice-Hall, Inc.,New Jersey, 1998.

Horne, R.H., Satik, C., Mahiya, G., Li, K., Ambusso, W., Tovar, R., Wang, C., and Nassori, H.: "Steam-Water Relative Permeability," *Proceedings of the World Geothermal Congress 2000*, Kyushu-Tohoku, Japan, May 28-June 10, 2000.

Kneafsy, T. J. and Pruess, K.: "Laboratory Experiments on Heat-Driven Two-Phase Flows in Natural and Artificial Rock Fractures," *Water Resources Research* Vol. 34, No. 12, December 1998, pp. 3349-3367.

Li, K. and Horne, R.N.: "Accurate Measurement of Steam Flow Properties," *Proceedings of Geothermal Resource Council*, Reno, California, USA, October 17-20, 1999.

Li, K. and Horne, R. N. (2001): "Characterization of Spontaneous Water Imbibition into Gas-Saturated Rocks," accepted to be published in *SPEJ* (2001).

Li, K. and Horne R.N.: "Differences between Steam-Water and Air-Water Capillary Pressures," *Proc.* of 26th Workshop on Geothermal Engineering, Stanford, CA, Jan. 29-31, 2001.

Lockhart, R. W. and Martinelli, R.C.: "Proposed Correction of Data for Isothermal Two-Phase Component Flow in Pipes," *Chem. Eng. Prog.*, Vol. 45, No. 39, 1949.

Ma, S., Morrow, N.R., and Zhang, X.: "Generalized Scaling of Spontaneous Imbibition Data for Strongly Water-Wet Systems," paper 95-138, presented at the 6th Petroleum Conference of the South Saskatchewan Section, the Petroleum Society of CIM, held in Regina, Saskatchewan, Canada, October 16-18, 1995.

Pan, X., Wong, R.C., and Maini, B.B.: Steady State Two-Phase Flow in a Smooth Parallel Fracture, presented at the 47th Annual Technical Meeting of the Petroleum Society in Calgary, Alberta, Canada, June 10-12, 1996.

Persoff, P. K., Pruess, K. and Myer, L.: "Two-Phase Flow Visualization and Relative Permeability Measurement in Transparent Replicas of Rough-Walled Rock Fractures," *Proceedings 16th Workshop on Geothermal Reservoir Engineering*, Stanford University, Stanford, California, January 23-25, 1991.

Persoff, P., and Pruess, K.: "Two-Phase Flow Visualization and Relative Permeability Measurement in Natural Rough-Walled Rock Fractures," *Water Resources Research* Vol. 31, No. 5, May, 1995, pp. 1175-1186.

Pruess, K., and Tsang, Y. W.: "On Two-Phase Relative Permeability and Capillary Pressure of Rough-Walled Rock Fractures," *Water Resources Research Vol*. 26 No. 9, September 1990, pp 1915-1926.

Scheidegger, A.E.: *The Physics of Flow Through Porous Media*, 3rd ed., University of Toronto, Toronto. 1974.

Su, G. W., Geller, J. T., Pruess, K. and Wen, F.: " Experimental Studies of Water Seepage and Intermittent Flow in Unsaturated, Rough-Walled Fractures," *Water Resources Research*, Vol. 35, No. 4, April 1999, pp. 1019-1037.

van Weereld, J.J.A., Player, M.A., Collie, D.A.L., and Olsen, D.: "Flow Imaging in Core Samples by Electrical Impedance Tomography, " SCA, June, 2001.

Witherspoon, P.A., Wang, J.S.W., Iwai, K. and Gale, J.E. : Validity of Cubic Law for Fluid Flow in a Deformable Rock Fracture, *Water Resources. Research*. Vol. 16, No. 6, 1980, pp 1016-1024.

Zhang, X., Morrow, N.R., and Ma, S.: "Experimental Verification of a Modified Scaling Group for Spontaneous Imbibition," *SPERE* (November 1996), 280-285.